Master Thesis

Observation of in-cloud vertical air motion with a combination of Doppler lidar, cloud radar and radar wind profiler

Results of the COLRAWI campaign

submitted by

Martin Radenz

Advisor:

Dr. Johannes Bühl

Reviewer:

Prof. Andreas Macke, Leibniz Institute for Tropospheric Research

RDir Dr. Volker Lehmann, Meteorological Observatory Lindenberg

Leipzig

February 26, 2017

Contents

1 Introduction

Clouds play a major role in the Earth's climate system (Bony et al. 2015). They change the radiative balance (Ramanathan et al. 1989) and are a key component of the hydrological cycle (Ramanathan et al. 2001). The formation of clouds and precipitation is still not well understood, especially not in a quantitative way. This lack of process level understanding causes large errors when clouds are modelled, either within climate simulation or weather prediction models (Williams and Tselioudis 2007).

Vertical air motion affects clouds in multiple ways. Within an updraft liquid cloud droplets may form, when cloud condensation nuclei (CCN) are present (Donner et al. 2016, Reutter et al. 2009 and Korolev and Field 2008). If the temperature is low enough, some particles act as ice nuclei (IN), the droplets freeze heterogeneously, making the cloud a mixed-phase cloud. Particle growth in a mixed phase cloud also depends on vertical air motion (Korolev 2007). Hence, cloud lifetime and ice production rate are very sensitively coupled to vertical motion (Korolev and Isaac 2003, Donner et al. 2016).

Probing clouds is inherently difficult. The range of covered temporal and spatial scales is tremendous. It reaches from the phase transition, acting on molecular scales, to the lifetime and extend of weather systems. Different measurement strategies are employed, for example in-situ measurements with aircraft, ground-based remote sensing or remote observations from satellites. In-situ measurements in the free troposphere are only available for short aircraft campaigns. They provide only a snapshot of the cloud along the flight path. Furthermore the invasive probing process may alter the cloud. Passive satellite observations cover the whole globe, but have a limited resolution and have poor vertical resolving power. Hence, the retrieved microphysical properties are an average over the satellites pixel and small scale variability is not covered. Ground based remote sensing instruments make high resolution, long term and cost efficient measurements possible and the gap between the scales of aircraft in-situ and satellite observations can be closed.

Cloudnet (Illingworth et al. 2007) is now a consortium of seven different European institutions that conduct long-term remote sensing observations. Today, it is part of the Aerosol, Clouds and Trace gases Research Infrastructure (ACTRIS). The core of Cloudnet is the synergistic processing of different ground-based remote sensing measurements with a standard algorithm (Illingworth et al. 2007). This algorithm requires at least a collocated cloud radar, a microwave radiometer and a ceilometer. The primary goal is to obtain a long term, quality controlled dataset for model evaluation. But the operational retrieval of products like liquid water content (LWC), ice water content (IWC) and particle velocity also allows detailed studies about cloud microphysics (Bühl et al. 2016). A clear advantage of Cloudnet is the provision of a dataset of vertically resolved cloud observations for up to a decade while several locations across Europe are covered.

As stated above, vertical air motions are a key driver of cloud microphysics. Hence, it is desirable to observe vertical air motions within this framework to get a holistic view on dynamical processes within clouds. Furthermore, the vertical velocity of a particle is the combination of the particle's terminal fall velocity and the velocity of the surrounding air. This holds under the assumption of stationary conditions. So, the vertical air velocity is required for an unbiased estimation of the terminal velocity. The spectrum of vertical velocities and information on the particle shape can then be used to obtain an quantitative insight into the ice production rate. So the knowledge of the vertical air velocity brings two insights: Firstly an important driver of cloud microphysics is directly observed. Secondly it allows the retrieval of the terminal particle velocity, which in a further step can provide an estimate of the clouds particle production rate.

Measuring clear air velocity remotely on cloud scale is difficult. Until now, no continuous and quality monitored remote observations of vertical air motion covering in-cloud and clear air are available. It is mostly done by observing tracers, like aerosol particles or cloud droplets, which are assumed to have a negligible velocity compared to the surrounding air (for example Shupe et al. 2008). But this is only feasible, when a sufficient concentration of these tracers is available. Furthermore it is hard to distinguish when a particle follows the air motion and when it moves relative to the air. radar wind profilers (RWPs) are the only well established instruments that can directly, i.e. without relying on tracers, observe vertical air motions by means of remote sensing (Van Zandt 2000). They are used operationally by meteorological services all over the world in order to obtain profiles of horizontal wind (Lehmann 2010). Besides that, they can be used to observe vertical motion in the free troposphere (Böhme et al. 2004) or precipitation (Gage et al. 1994, Orr and Martner 1996). However, as RWPs are common radars, they are not only sensitive to clear air return. Large particles, also add particle scattering to the signal. The effect, that a RWP is sensitive to both signals is commonly called wind profiler ambiguity (Knight and Miller 1998). This ambiguity hampers any effort to observe vertical motion within clouds.

One further advantage of RWPs is their long wavelength. Contrary to shorter wavelength radars, they suffer less from attenuation. Especially millimeter wavelength cloud radars, which are commonly used for cloud microphysics studies are susceptible to strong attenuation, caused by many large particles which are confined inside the beam volume. Within convective clouds attenuation becomes a serious problem. RWPs can help to diminish this gap in remote sensing observations.

At the Meteorological Observatory Lindenberg (MOL) an extensive set of in-situ and ground-based remote sensing instruments is operated by the German Meteorological Service (Deutscher Wetterdienst - DWD). For more than ten years MOL has been a member of the Cloudnet consortium. The measurements from a 35 GHz cloud radar, a multichannel microwave radiometer and a ceilometer are already processed by the standard algorithm. What makes MOL unique, is the collocated powerful 482 MHz RWP. Routinely it is used for the assimilation of horizontal wind profiles to numerical weather prediction (NWP) models. Additionally a Doppler lidar is available at the site.

Aim of this thesis is to combine measurements of cloud radar, RWP and Doppler lidar in order to derive continuous measurements of vertical air velocity in clouds that are unbiased by cloud particles. An algorithm for correction of the wind profiler ambiguity is developed, implemented and tested. For an automated data processing, quality control is indispensable. A scheme for the estimation of a quality flag is also developed and implemented. The resulting vertical air velocity dataset is incorporated into Cloudnet. For the first time continuous observations of clear air and in-cloud vertical motion in the free troposphere are included in such a framework.

In this work, a novel combination of a powerful 482 MHz RWP, a 35 GHz cloud radar and a Doppler lidar is used. The data was recorded during the COLRAWI campaigns (Combined observations with lidar, radar and wind profiler) in 2013 and 2015.

A combination of multiple frequencies has been done before. For example Williams et al. (2000) or Gage et al. (1999) used the combination of two RWPs to discriminate particulate from clear air signal. Recently, Williams (2012) showed that correction of the wind profiler ambiguity is possible by combining the spectra a 920 MHz and a 50 MHz RWP. In this thesis, a combination of a RWP with a millimeter wavelength cloud radar is used. The cloud radar has the specific advantage that it is only sensitive to particles and does not show any influence of Bragg scattering. Hence, it provides the pure complimentary information to remove the particle influence from the RWP signal.

In the following chapter, a brief introduction into the theory of atmospheric scattering and active remote sensing is given. Further on, the combination of RWP and cloud radar spectra is explained. Within the forth chapter the results of the algorithm are explored. The capabilities of the combination and the correction algorithm are illustrated by case studies. A comparison with the ICON (icosahedral nonhydrostatic) model is presented and some long term statistics are shown. The accomplished insights to vertical air motion are briefly summarized and a outlook on future work is given.

2 Theory

Observing the clouds and aerosols remotely requires complex instrumentation. To understand how radar and lidar systems work and how their measurements can be combined requires some theoretical background. At first, some basic equation for active remote sensing and atmospheric turbulence are introduced. After that, different scattering processes are covered and it is shown how they interact at different wavelengths. To observe motion via the Doppler effect, the instruments emit coherent radiation. The design and signal processing of those systems is presented. In the end some processes that introduce artificial effects on the velocity spectrum are discussed.

2.1 Basic principle of radar and lidar

Using remote sensing, we want to obtain information from a volume which is separated from the instrument geometrically. This can be done either by active or passive methods. The basic principle of the two active systems, radar (radio detection and ranging) and lidar (light detection and ranging) is quite comparable. A pulse of electromagnetic energy is emitted into the atmosphere. A portion of this pulse is eventually scattered back to the instrument, where it is received. The range of the scattering process is calculated from the time between pulse emission and detection. The received power P_r is described by the radar equation, here given in its simplest form (Rinehart 1991):

$$P_r(r) = \frac{C_r}{r^2}\,\tau(r)^2\,\eta(r) \tag{2.1}$$

with the Radar system parameter C_r, the range r, the transmissivity τ and the reflectivity η. The system parameter contains all instrument-specific information about antenna gain, pulse power and pulse duration and antenna pattern. The reflectivity η is the sum of all backscattering cross sections σ_b inside a unit volume:

$$\eta(z) = \sum_i \sigma_{b,i} \tag{2.2}$$

The radar receives only the backscattered portion of the radiation. In general the energy is scattered into all directions. So a portion of the energy leaves the beam and weakens the pulse. Absorption by condensed water and atmospheric gases removes energy from the pulse, too. How severe this attenuation is depends on the system. Lidars can be attenuated by clouds, whereas for cloud radars strong precipitation is required. In light precipitation and for long wavelengths attenuation can usually be neglected and $\tau(r) = 1$.

The reflectivity η is commonly expressed as the equivalent reflectivity factor z_e in linear representation (Rinehart 1991):

$$z_e = \frac{\eta \lambda^4}{\pi^5 |K|^2} = \sum_i N_i D_i^6 \qquad (2.3)$$

with

$$|K|^2 = \left(\frac{n^2 - 1}{n^2 + 2}\right)^2 \qquad (2.4)$$

Usually the refractive index for liquid water is used, neglecting the actual phase. Within this thesis all reflectivity factors are equivalent reflectivity factors, the subscribt e is omitted. As z spans over several magnitudes it is usually given logarithmically:

$$Z = 10 \log_{10} (z/z_0) \qquad (2.5)$$

with $z_0 = 1\,\mathrm{mm}^6\,\mathrm{m}^{-3}$. The unit of Z in logarithmic representation is dBZ.

2.2 Turbulence

Kinetic energy in the atmosphere is generated at large scales due to convection caused by differential heating, wind shear or gravity waves. For example, when an air parcel is heated at the Earth's surface, gets buoyant and starts to ascend. To conserve mass a descending counterflow develops elsewhere. An initial eddy has developed. The large eddies break up into smaller and smaller ones and the kinetic energy is distributed among them. The turbulent energy is transported through the scaled until it dissolves at the smallest scale, the Kolmogorov microscale (Kolmogorov 1941). The power spectrum of the energy is given by

$$E(k) = C \epsilon^{\frac{2}{3}} k^{-\frac{5}{3}} \qquad (2.6)$$

where $C \approx 0.5$ is the Kolmogorov constant, ϵ is the energy dissipation rate and $k = \frac{2\pi}{l}$ the wavenumber. The part of the spectrum, that follows the $-\frac{5}{3}$ power law is called inertial subrange. Within this region the turbulence is assumed to be isotropic. The link from temporal frequencies (as in the measurements) to spatial frequencies can be done using Taylor's hypothesis, which states that the eddies are advected over the instrument by the mean flow: $k = \frac{2\pi}{u_a} f$. An example for such a turbulence spectrum is shown in figure 2.1. Here, the inertial subrange begins at roughly $500\,\mathrm{m}$. At wavelengths shorter than approximately $10\,\mathrm{m}$ the noise of the measurement system masks the inertial subrange.
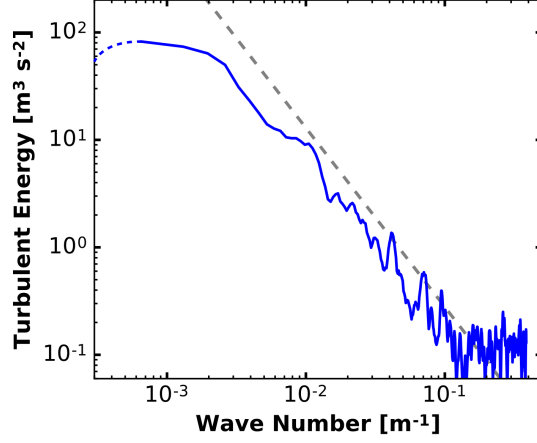
Fig. 2.1: Example for a turbulence spectrum measured with a Doppler lidar within the PBL. The theoretical $-\frac{5}{3}$ slope is marked by a dashed line.

2.3 Scattering in the atmosphere

Active remote sensing relies on scattered energy. Different scattering processes can be distinguished. Within this section, scattering by particles is treated firstly. After that, clear air scattering caused by fluctuations of the refractive index is introduced. Depending on the wavelength, the strength of each scattering process varies. This is treated in the last part of this section. In principal the discussed scattering mechanisms are general for all wavelengths, but we focus on the region from millimeter to meter wavelengths.

2.3.1 Scattering by spheres

The backscattering cross section σ_b of a spherical particle with a given diameter D_p is given by Lorenz-Mie Theory (Bohren and Huffman 2008). It depends on the size parameter $x = \pi D_p / \lambda$ and the complex refractive index $n = n_r + i\, n_i$ of the particle. Where λ is the wavelength of the electromagnetic radiation, $n_r = \mathrm{Re}(n)$ and $n_i = \mathrm{Im}(n)$. There is no straightforward analytical solution for σ_b, for a particular particle it has to be computed numerically or looked up in tables. Multiple particles inside a unit volume contribute to the reflectivity η independently. The reflectivities can be summed up according to equation 2.2 if the phases of the scattered waves from the single particles are random. This is valid for homogeneously filled beam volumes.

2.3.2 Rayleigh approximation

When the particle diameter is small compared to the wavelength ($x < 0.2$), the simpler Rayleigh approximation can be used.

$$\eta_R(z) = \frac{\pi^5 |K|^2}{\lambda^4} \sum_i N_i D_i^6 \tag{2.7}$$

The refractive index varies with wavelength, so does $|K|^2$ (see equation 2.4). This variability can be parametrized. Here, the widely used parametrization given by Ray
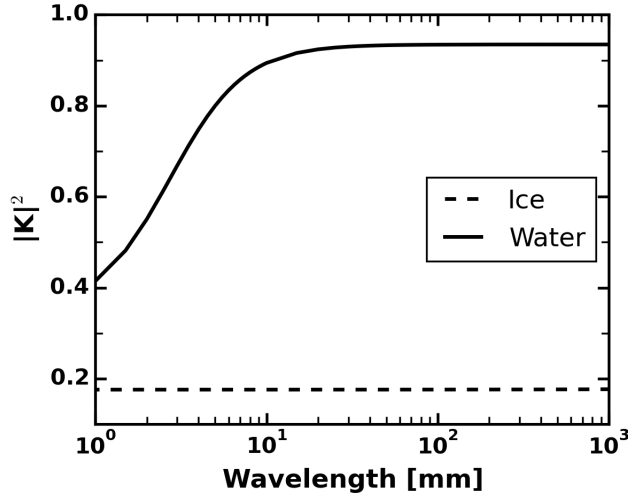
Fig. 2.2: Dependancy of $|K|^2$ on the wavelength for a Temperature of 0°C.

(1972) is used. For ice, the wavelength dependency is negligible $|K|^2 \approx 0.176$ (at these wavelengths). For water $|K|^2$ converges to 0.93 for long wavelengths (figure 2.2).

An important constraint of the Rayleigh approximation (as for Lorenz-Mie theory above) is, that the particles have to be randomly distributed within the pulse volume. As Matsuda et al. (2014) and Argyrouli et al. (2012) suggested, the return of clustered scatterers can be significantly lower than predicted by this approximation.

Within the PBL additional backscattering can be caused by insects, birds and other atmospheric plankton. This signal can easily be discriminated from „real" atmospheric scattering by its depolarization characteristics (Bauer-Pfundstein and Görsdorf 2007) as the scatterers are not spherical.

2.3.3 Bragg scattering

Clear air scattering or Bragg scattering is caused by inhomogeneities of the refractive index of clear air. Air parcels with different temperature and/or humidity are mixed by turbulence. This mixing causes refractive index gradients within the inertial subrange. It is common to express the refractive index n as refractivity $N = (n - 1) \cdot 10^6$. A parametrization of the refractivity is given by Doviak and Zrnic (1993):

$$N = c_1 \frac{p}{T} + c_2 \frac{e}{T} + c_3 \frac{e}{T^2} \tag{2.8}$$

with $c_1 = 0.776 \, \mathrm{K \, Pa^{-1}}$, $c_2 = 0.716 \, \mathrm{K \, Pa^{-1}}$ and $c_3 = 3.7 \cdot 10^3 \, \mathrm{K^2 \, Pa^{-1}}$ where T is the temperature, p the pressure and e the water vapor partial pressure. Air parcels of different refractive index (i.e. different temperature or humidity) are mixed by turbulence causing refractive index gradients at different scales in the otherwise „clear" air. The reflectivity of a volume is (Hardy et al. 1966, Ottersten 1969)

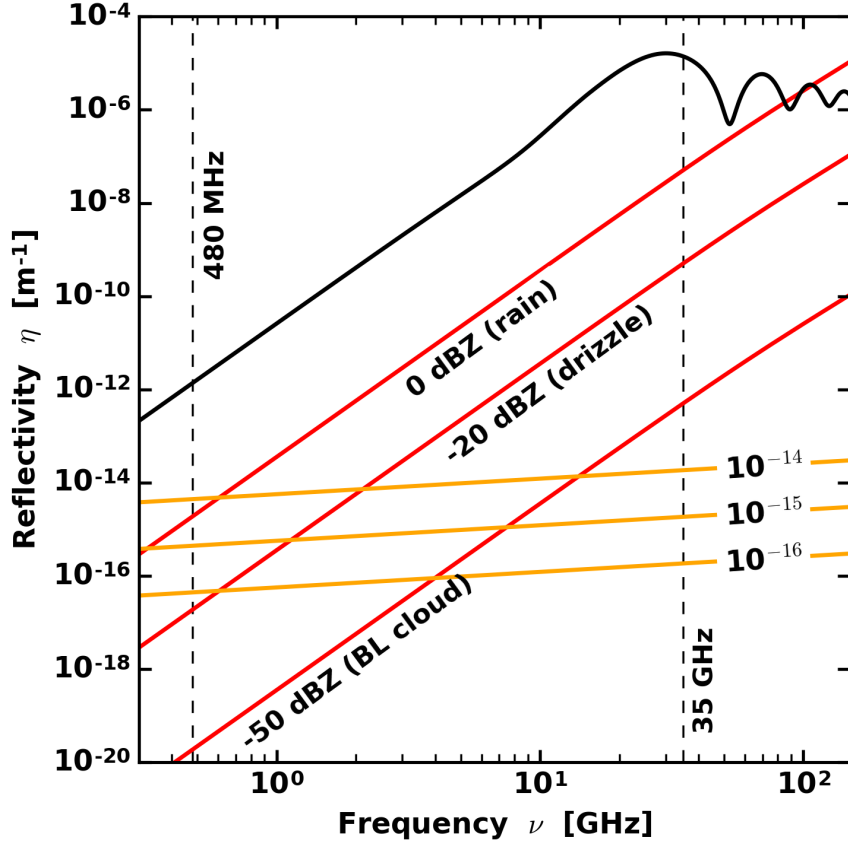$$\eta_B(z) = 0.38 \, C_n^2 \, \lambda^{-1/3} \tag{2.9}$$

Fig. 2.3: Reflectivity η for different scattering processes. The black line is calculated for droplets with $d = 3\,\text{mm}$ and $N = 1\,\text{m}^{-3}$. Red lines denote the reflectivity for the Rayleigh approximation: $0\,\text{dBZ}$ corresponds to $N = 1\,\text{m}^{-3}$ with $d = 1\,\text{mm}$, $-20\,\text{dBZ}$ to $N = 150\,\text{m}^{-3}$ with $d = 200\,\mu\text{m}$ and $-50\,\text{dBZ}$ to $N = 150000\,\text{m}^{-3}$ with $d = 20\,\mu\text{m}$. The reflectivity of Bragg scattering is given in orange for different intensities of turbulence C_n^2 in $[\text{m}^{-2/3}]$

with the refractive index structure constant C_n^2. It can be understood as the fluctuation of the refractive index Δn (Hardy et al. 1966)

$$C_n^2 = 5.26\,\overline{(\Delta n^2)}\,L_0^{-2/3}. \tag{2.10}$$

where L_0 is the outer range of the inertial subrange as introduced in section 2.2. The strongest contribution to η_B is made by eddies with a diameter of half the wavelength. Most of the time the turbulence at this scales is within the inertial subrange and therefore isotropic. Bragg scattering is not necessarily isotropic, as refractive index gradients can have a large horizontal extend, i.e. at the top of the PBL where humidity decreases rapidly.

2.3.4 Combined scattering

The individual contribution of Rayleigh, Mie and Bragg scattering varies between different radar instruments depending on the wavelength at which they operate. Figure 2.3 shows this for different scenarios. For short wavelengths particulate scattering prevails.

For wavelengths longer than ten centimeters (approximately 3 GHz), Bragg scattering can be as strong as particulate scattering (Fig. 2.3). This causes the so called wind profiler ambiguity, where the signal from particles and clear air is equal in magnitude and can't be easily distinguished (Knight and Miller 1998). The wind profiler ambiguity is a known issue in the wind profiler community and several approaches are available to address it. For example Orr and Martner (1996) used observations at two frequencies and height dependant thresholds of reflectivity and velocity to detect particle influence. Gage et al. (1999) used differential reflectivity to diagnose which scattering is dominant.

2.4 Particle vertical motion

Particles move through the atmosphere either due to acceleration by the surrounding air or due to gravity. The motion of the particle relative to the surrounding are is called terminal (fall) velocity. The magnitude depends on a particle's shape and mass. If the shape is known, the mass can be related to the size using laboratory and in-situ measurements (Mitchell 1996, Heymsfield and Westbrook 2010). This has two consequences: Firstly very small particles (approximately less than $50\,\mu$m) have negligible terminal fall velocities and can be regarded as an air motion tracer. Secondly, if the shape is known, the size can be retrieved from the terminal fall velocity.

The shape of the particle can be inferred or measured, e.g. by using polarimetric cloud radars (Reinking et al. 1997, Myagkov et al. 2016, Bühl et al. 2016). From ground, the particle fall velocity is measured with respect to the earth fixed coordinate system (Section 2.5). When the vertical air motion is known and assuming stationary conditions, the terminal fall velocity can be calculated. Afterwards the terminal velocity can be linked to the particle size (Fig. 2.4) using the laboratory data.
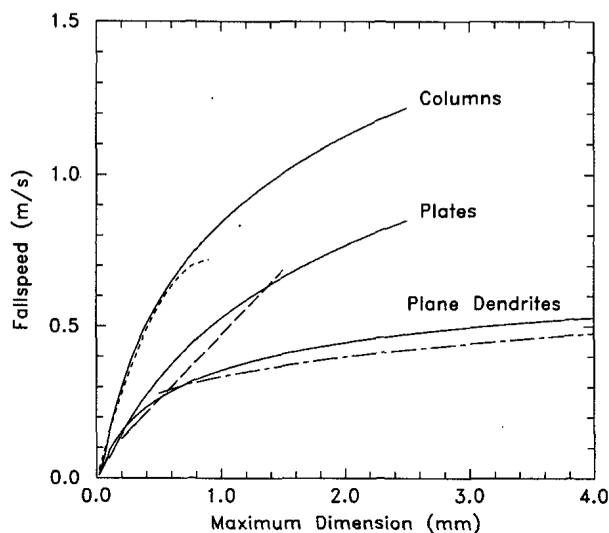

Fig. 2.4: Terminal velocity of different ice crystal shapes depending on maximum dimension from Mitchells theory (solid) and for emperical expressions (dashed). Image credit: Mitchell 1996

10

2.5 Coherent systems and Doppler spectra

As shown above, particles move vertically, driven by air motion or their own weight. When these particles interact with a pulse of electromagnetic energy, the phase of the scattered pulse is slightly shifted. The magnitude of this shift depends on the particle's motion radial to the beam. The phase shift over time can be understood as a frequency shift, which is commonly referred as Doppler effect. Depending on the instruments wavelength the shift within one pulse or between successive pulses is used. Former is done by Doppler Lidars, latter typically by radars. Prerequisite for the detection of phase shifts is a coherent design, that means the phase of the emitted pulse has to be known and the phase of received pulse has to be measured. The Radar signal processing is described in the following. For further details refer to the general text of Doviak and Zrnic (1993) or the cloud radar specific one of Görsdorf et al. (2015). An overview on Doppler Lidar is given by Werner (2005) or more specific by Pearson et al. (2009), here only some relevant details are mentioned.

Basically the signal processing of the cloud radar and the RWP are identically. They only differ in specific technical aspects, like for example how many intermedient frequencies (IFs) are necessary. High frequencies cannot be sampled directly, therefore the signal is mixed with a local oscillator of nearly the same frequency. The envelope of the resulting beat can be sampled at lower frequencies. This frequency reduction can be repeated. The total number of IFs depends on the radars operating frequency.

The atmospheric signal is represented as the discrete, complex series $\underline{s}(t) = I(t) + iQ(t)$. For each pulse and range gate a pair of *I-Q* data is sampled, where I is the in phase part and Q is the $90°$ shifted quadrature part of the signal. This is necessary to capture not only the amplitude but also the phase of the signal. The underline denotes a complex variable. This signal is the composition of particulate scattering a_p, Bragg scattering a_B, clutter c and noise n (Muschinski et al. 2005):

$$\underline{s}(t) = \underline{a}_p(t) + \underline{a}_B(t) + \underline{c}(t) + \underline{n}(t) \tag{2.11}$$

After sampling a number of N_{FFT} pulses, a fast Fourier transform is applied on the sequence of $\underline{s}$. This gives a complex spectrum $\underline{\hat{s}}(v_k)$ where the frequency shift can be linked to the radial velocity:

$$\Delta f_k = -\frac{2\,v_k}{\lambda} \tag{2.12}$$

The periodogram is calculated as the absolute value squared or:

$$\hat{s}(v_k) = \underline{\hat{s}}(v_k)\,\underline{\hat{s}}^*(v_k) \tag{2.13}$$

where $*$ denotes the complex conjugate. These periodograms are noisy (Muschinski et al. 2005). If the signal is stationary over a reasonable long time, these periodograms can be averaged incoherently to get a smoother estimate of the power spectrum. This power spectrum is commonly called Doppler spectrum.
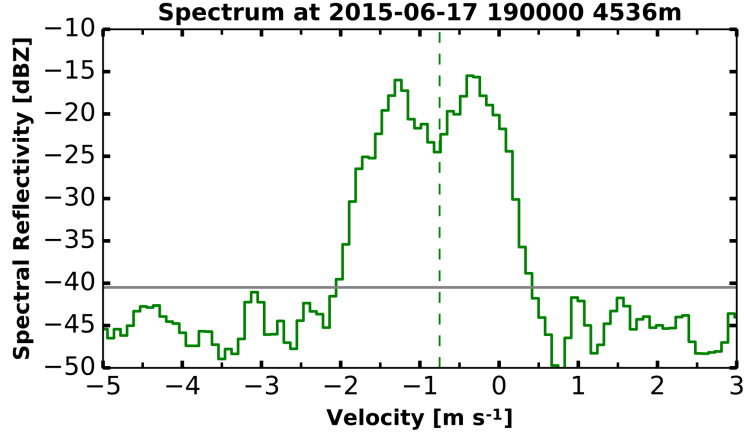
Fig. 2.5: Example for a measured Doppler spectrum with two peaks. The left peak is caused by ice particles and the right one by Bragg scattering. At this height, the noise level lies around $-45\,\mathrm{dBZ}$ with the noise threshold marked in gray. The reflectivity weighted mean velocity is marked with a dashed line.

Each spectrum contains the velocity distribution of scatterers in the observed volume, weighted by the received power for each range gate and time step. The single contributions in 2.11 are still additive in the frequency representation, if the processes are independent of each other: $\langle \underline{\hat{a}}\, \underline{\hat{n}}^* \rangle = 0$, $\langle \underline{\hat{a}}\, \underline{\hat{c}}^* \rangle = 0$. With the expectation value $\langle . \rangle = 0$ over the sample. Especially this has to be true for $\langle \underline{\hat{a}}_p\, \underline{\hat{a}}_B^* \rangle = 0$ (C. Williams, personal communication). The resolution of the spectrum is determined by the Nyquist frequency $f_n = \lambda\,\mathrm{PRF}/4$ and N_{FFT}.

The peaks in this spectrum represent the different returns from particles and clear-air (Bragg) scattering. An example for such a spectrum is shown in Fig. 2.5. But as noted by Giangrande et al. (2001) the interpretation of the spectra has to be done with great caution, as the incoherent averaging may introduce artificial peaks. The noise level $\hat{n}$ is usually determined by the Hildebrand-Sekhon algorithm (Hildebrand and Sekhon 1974). Traditionally only the first three moments of the whole spectrum are calculated and stored:

$$P_r = \sum_{v_k = v_1}^{v_2} \left[\hat{s}\left(v_k \right) - \hat{n} \right] \tag{2.14}$$

$$\overline{v} = \frac{1}{P_r} \sum_{v_k = v_1}^{v_2} v_k \left[\hat{s}\left(v_k \right) - \hat{n} \right] \tag{2.15}$$

$$\sigma^2 = \frac{1}{P_r} \sum_{v_k = v_1}^{v_2} \left(v_k - \overline{v} \right)^2 \left[\hat{s}\left(v_k \right) - \hat{n} \right] \tag{2.16}$$

An example for $\bar{v}$ from a RWP measurement is shown in Fig. 2.6. Here the windprofiler ambiguity becomes strikingly evident. During the first 4 hours, the clear air signal prevails and a alternating of up- and downward motion can be observed. But, as a frontal zone in moving in, the scene becomes more and more dominated by clouds. The strong signal form falling particles masks the contribution of the Bragg scattering completely.
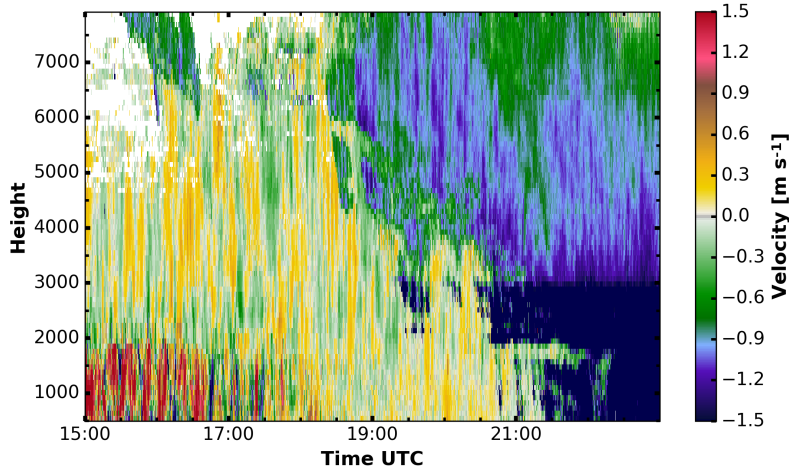

Fig. 2.6: Example for the vertical velocity retrieved with the standard RWP signal processing. Details of this processing are covered later.

Coherent lidar systems operate in a quite comparable manner. Most Doppler lidars for tropospheric applications are pulsed systems with heterodyne detection (Pearson et al. 2009). For precise measurements of vertical velocity some special issues have to be taken into account. If the range gate length is smaller than the pulse length, the chirp effect becomes visible. The chirp effect is caused by a change in the frequency within the emitted pulse and introduces a bias to the measured velocity. The magnitude of this bias depends on the shape of pulses spectrum. If the pulse spectrum is measured, the effect can be corrected by a two-dimensional deconvolution (Bühl et al. 2012).

2.6 Influence of air motion on spectra

Air motion affects the Doppler spectrum sampled by a radar. The spectrum can be broadened, for example due to:

- incoherent averaging over non stationary signals
- sub-scale turbulence (Shupe et al. 2008)
- beam geometry (Nastrom 1997)

The drop size distribution and the sub scale turbulence are assumed to be equal for the both radars used here and can therefore be neglected. The beam geometry effects have to be considered. At the edges the beam is not exactly vertical and a small component of the horizontal vector contributes to the vertical velocity.

Nastrom (1997) derived a formula which incorporates the effects of beamwidth and wind shear. To make physical interpretation possible, the power series expansion of the exact formula is given here (Nastrom 1997):

$$
\begin{aligned}
\sigma_b^2 \approx \quad & \frac{\vartheta^2}{3} u_0^2 \cos^2 \alpha && \text{(I)} \\
& - \frac{2\vartheta^2}{3} \sin^2 \alpha \left(u_0 \frac{\partial u}{\partial z} R_0 \cos \alpha \right) && \text{(II)} \\
& + \frac{\vartheta^2}{24} \left(3 + \cos 4\alpha - 4\cos 2\alpha \right) \left(\frac{\partial u}{\partial z} \right)^2 R_0^2 && \text{(III)} \\
& + \left(\frac{\vartheta^2}{3} \cos 4\alpha + \sin^2 \alpha \cos^2 \alpha \right) \left(\frac{\partial u}{\partial z} \right)^2 \frac{\Delta R^2}{12} && \text{(IV)}
\end{aligned}
\tag{2.17}
$$

with $\Gamma_n = \sin(n\vartheta)/(n\vartheta)$, the half-beamwidth ϑ, the zenith angle α, the range R_0, the range gate length ΔR, the horizontal wind velocity u_0 and the vertical shear of the horizontal wind $\partial u/\partial z$. Within this work only the broadening of vertical beams is of importance, so $\alpha = 0$ and some terms simplify further. The first term in (I) represents the direct effect of the horizontal wind within the volume and depends only on the beamwidth. The second term describes the first order effects of shear for slanted beams. The further terms describe the combined effects of beamwidth and wind shear. The range dependent effects are covered by term (III), whereas the pulse length is relevant in (IV). The amount of broadening for different conditions is shown in Fig. 2.7. Due to the larger observation volume (beamwidth and pulse length) of the RWP it is nearly twice as high as for the cloud radar.

Additionally to the broadening effect, air motion can also cause a bias in the observed vertical velocity:

- vertical air motion (at scales larger than the beam volume)
- intermittency flux (Muschinski and Sullivan 2013)
- incorrect vertical alignment

The first effect is only relevant if particles are observed (i.e. with the cloud radar). It can be corrected, if the vertical air velocity is measured otherwise (see section 2.4) or if it is averaged over a full up- and downdraft cycle.

Intermittency fluxes are caused by covariances of the reflectivity and the vertical velocity in a turbulent field. They cause a bias between the air velocity and the observed Doppler velocity. Within the PBL this bias can reach $-0.5\,\mathrm{m\,s^{-1}}$, but should be smaller in the free troposphere (Muschinski and Sullivan 2013).

The alignment of the antenna is more crucial. If it is not pointed directly towards the vertical, horizontal wind will introduce a bias in the measurement of the vertical velocity (Fig. 2.8). The magnitude of this bias depends on horizontal wind speed and the sign on the wind direction. This bias is hard to detect in the in the measurements, as the magnitude depends on wind direction and the direction of the antenna misalignment.
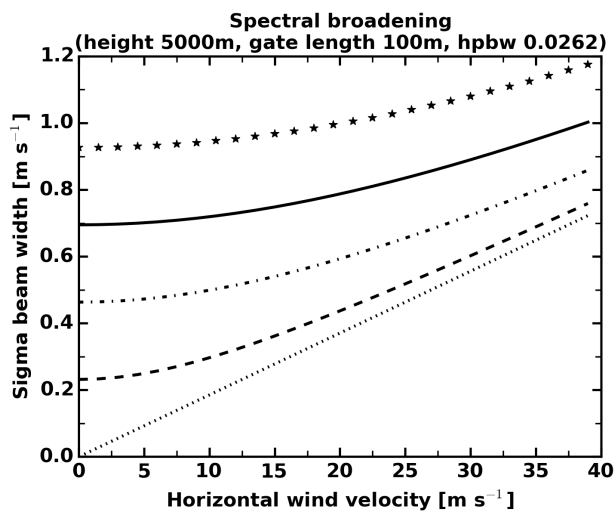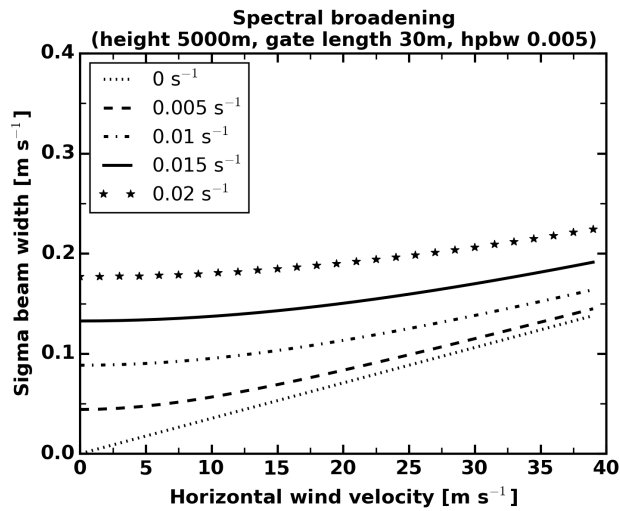
**Spectral broadening
(height 5000m, gate length 30m, hpbw 0.005)**

Legend:
- ⋯⋯ $0\ s^{-1}$
- – – $0.005\ s^{-1}$
- –·–· $0.01\ s^{-1}$
- —— $0.015\ s^{-1}$
- ★ ★ $0.02\ s^{-1}$

Sigma beam width [m s^{-1}] vs. Horizontal wind velocity [m s^{-1}]

**Spectral broadening
(height 5000m, gate length 100m, hpbw 0.0262)**

Sigma beam width [m s^{-1}] vs. Horizontal wind velocity [m s^{-1}]

Fig. 2.7: Beam width broadening σ_b of cloud radar (top) and RWP (bottom) for different horizontal velocities and wind shear at 5 km height. The parameters are slightly idealized compared to the instruments introduced in chapter 3. The legend is valid for both plots, but the ordinate differs.
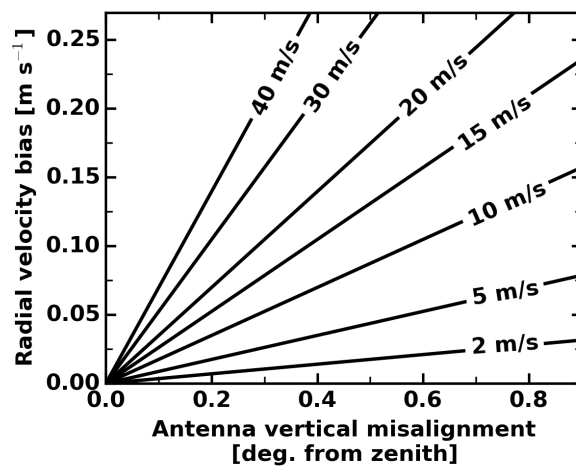

Fig. 2.8: Bias in the vertical velocity due to antenna misalignment for different horizontal velocities.

3 A new suite of instruments: Combination of cloud radar, radar wind profiler and Doppler lidar

The proposed combination gives novel insights to vertical motion, but several technical issues have to be considered. At first a brief summary on the used instruments, their technical details and the measurement campaign is provided. Afterwards, the algorithm for the correction of the particle influence is comprehensively described. An overview of the correction algorithm is presented in section 3.2. Further on, its key parts are explained in detail. The first step is a relative calibration of the two systems. As an auxiliary information, the profile of the horizontal wind is needed. Several sources, that can provide such a profile are described in the forth section. A flag is used to assess the quality of each spectrum. The criteria is described in the next section. Further on, the correction itself is treated. Three methods are described in detail and are evaluated afterwards.

3.1 Measurement instruments at Lindenberg

The measurements used in this study were taken at MOL by the German Meteorological Service (Deutscher Wetterdienst - DWD) during the COLRAWI campaign (Bühl et al. 2015). The campaign took place in two phases, the first covering several days in summer 2013. A second phase took place between June and September 2015.

At Lindenberg, a rare collection of remote and in-situ instruments is operated by the DWD. Amongst others, a 482 MHz RWP (Böhme et al. 2004), a MIRA-35 cloud radar (Görsdorf et al. 2015), a 1.55 µm Streamline Doppler wind lidar (Pearson et al. 2009) and a ultra-violet Raman lidar (Reichardt et al. 2012). Powerful RWPs at the lower edge of UHF band with a narrow beamwidth are rare because of high costs (in a technical and personnel sense). The collocation with a sophisticated cloud radar is even rarer.

In the following chapters, the term "RWP" refers to the 482 MHz Radar and "cloud radar" to the 35 GHz system. But in general, the methods presented in this work are not restricted to these frequencies. The technical parameters of the major instruments are given in table 3.1.

Cloud radar and Doppler lidar were operated in a vertical only mode. The RWP had two operation modes. One, called „intermittent" mode, with alternating advection scans and vertical observation, each lasting 30 minutes. This mode was used for most of the time to fulfill the requirements for operational delivery of horizontal wind profiles. The second one with vertical only measurements was used during intensive observation periods (IOPs), i.e. when interesting meteorological conditions like frontal passages and convective precipitation were present.

As introduced in section 2.5, Doppler lidars may suffer from a velocity bias. For the Streamline Doppler lidar this bias could not be corrected, because no measurements of the pulse spectrum are available (Bühl 2015).

	RWP	Cloud Radar	Doppler lidar
Type	LAP 16000	MIRA 35	Streamline
Wavelength	0.62 m	8.5 mm	1.5 μm
Beam Width	2.9°	0.58°	0.03°
Range Gate Length	94 m	30 m	48 m
Pulse Length	1 μs	200 ns	160 ns
Integration Time	10 s	10 s	2 s
No. Incoherent Averages	4, 3	200	30000
Pulse Repetition Frequency	12.2, 10.0 kHz	5 kHz	15 kHz
Average Emitted Power	200 W	30 W	200 mW
N_{FFT}	512	256	-

Table 3.1: Properties of the major instruments used in the COLRAWI campaigns (based on Bühl et al. 2015). The second values for the RWP are settings during IOPs.

3.2 Development of a new algorithm to remove particle influence from RWP

The algorithm for the correction of the particle influence requires several steps. An overview is provided in Fig. 3.1. The basic idea is, that particulate and Bragg scattering contribute independently to the received power of the RWP. Having information from a second radar, that is more sensitive to particle return, both scattering processes can be separated in the RWP measurement. Here ca cloud radar is used to provide the information on the particle contribution. Such an approach was used by (Williams 2012), who combined a 920 MHz and a 50 MHz radar. This gives a frequency separation factor of 18. In this study a 35 GHz and a 482 MHz (factor 73) radar are combined. A larger factor allows a better discrimination of both scattering processes.

The first step in the correction process is to calibrate both radars relative to each other. Without this the spectra produced by both radars cannot be compared in a quantitative manner. The calibration is covered in the following section. As shown in chapter 2.6, the horizontal wind affects the spectra. To incorporate this effects, the profile of the horizontal wind is required. Three sources are reviewed. To assess the the quality of each spectrum, a integer value flag is used. The decision logic and the thresholds were developed and are described in the corresponding section. Afterwards the correction methods, which are the core of whole algorithm, are discussed. Three methods are proposed and evaluated using a Monte Carlo simulation with artificial spectra.
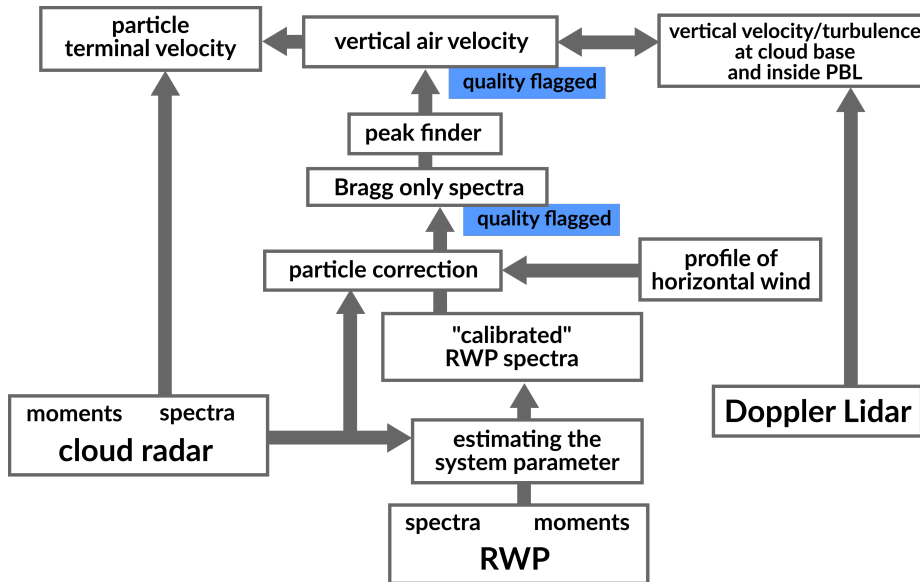
Fig. 3.1: Scheme of the correction software „spectra mole". The spectra and moments from the standard data processing are loaded from the netcdf-files. The spectra from the wind profiler and the cloud radar are then combined to cross calibrate the wind profiler and correct the particle influence. Finally, the vertical air velocity is estimated. Using again the cloud radar information, the terminal velocity is calculated.

3.3 Relative calibration of cloud radar and RWP

A relative calibration between both instruments is necessary for the removal of the particle signal from the RWP spectra. Usually the RWP is not absolutely calibrated and only the velocity information is used. This calibration means, that the factor C_r in formula 2.1 needs to be estimated. This factor is called system parameter within this work. The system parameter is estimated by comparing the spectra of the cloud radar and the RWP in regions were the backscattered signal is expected to be equal for both systems. This is the case for light rain and small ice crystals, for which the Rayleigh approximation is valid. Then the reflectivity factor Z is independent of the wavelength and therefore equal for both RWP and cloud radar.

A restricted spectral band between $-3.0\,\mathrm{m\,s^{-1}}$ and $-0.9\,\mathrm{m\,s^{-1}}$ is used to (Fig. 3.2). This is done to exclude the Bragg signal, which is for most cases in the proximity of $0\,\mathrm{m\,s^{-1}}$, and non Rayleigh scattering from larger hydrometeors with large falling velocities. From the difference in the backscattered signal between cloud radar and RWP within this band, the system parameter is calculated.

Orr and Martner (1996) applied a similar approach by using the 0th moment (i.e. the full spectrum) within light rain events. Their approach has two shortcomings. Firstly homogeneous light rain events have to be reasonable frequent and have to be selected manually. Secondly, if the 0th moment is computed over the whole peak, a Bragg contribution is mixed into the signal to noise ratio (SNR) of the RWP.

C_r can be estimated within a wide range of atmospheric conditions, as long as particles that show Rayleigh scattering for at both 35 GHz and 482 MHz are present. This allows a continuous monitoring of the relative fluctuation of the relative calibration (Fig. 3.3).
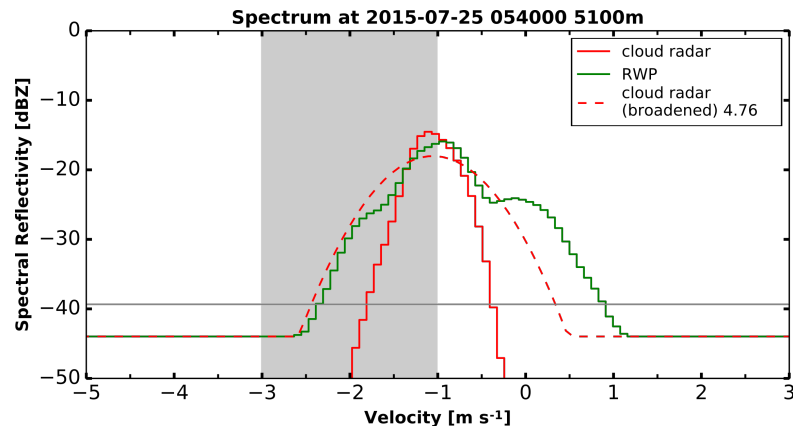

Fig. 3.2: Spectrum from the 25th July 2015 0540 UTC at 5100 m illustrating the calculation of the system parameter. The spectral range used is denoted in grey. The secondary peak at $0.2 \, \mathrm{m\,s^{-1}}$ is caused by Bragg scattering.

The antennas of all instruments have to be aligned very accurately to the vertical direction. The RWP antenna, which is mounted on a solid steel frame is assumed to be aligned without bias. The cloud radar is housed in a mobile trailer, the accuracy is around $0.25°$ (U. Görsdorf, personal communication). For typical atmospheric conditions the bias should not exceed $0.12 \, \mathrm{m\,s^{-1}}$ (Fig. 2.8).
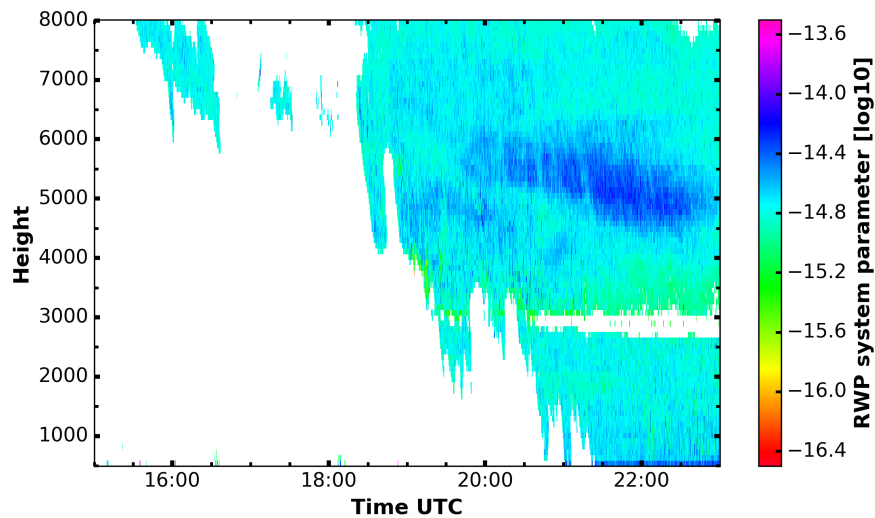

Fig. 3.3: Estimated system parameter during the evening of the 17 June 2015 (same period as example in section 4.2.1).

3.4 Determining the horizontal wind

High resolution horizontal wind profiles are a crucial piece of information for understanding the measurement, as depicted in section 2.6. The resolution has to be close to the vertical extend of turbulent layers, as shear of the horizontal wind drives such layers. For a spectral combination of instruments a resolution of one hundred meters or less is desirable. Several measurement systems allow the retrieval of such profiles:

- **Radiosonde:** Using the drift of an ascending weather balloon, the horizontal wind profile can be estimated. At Lindenberg those ascends are conducted every 6 hours. The vertical resolution depends on the ascend speed of the radiosonde and is around 200 m. Beside the sparse temporal resolution (6 to 12 hours between two ascends under operational conditions), the dislocation of the balloon is a problem. Distances up to several hundred kilometres may occur.

- **Cloudnet Model Data:** Inside the Cloudnet algorithm the horizontal wind data from operational NWP models is used. Most commonly is the Integrated Forecasting System by the European Center for Medium-Range Weather Forecast (ECMWF). As most models use pressure as a vertical coordinate, the heights are not evenly spaced. In the planetary boundary layer intervals of 100 m are common, whereas in the upper troposphere they increase to 500 m and more. The temporal resolution is between 1 and 6 hours.

- **RWP:** Radial velocities from RWP off-zenith beam can be used to calculate a profile of horizontal wind (Balsley and Gage 1982, Woodman and Guillen 1974). Sampling of such a profile requires roughly half an hour and the vertical resolution is determined by the RWP itself. In our case the range gate spacing is 93 m. During the COLRAWI campaign off-zenith measurements were only done in 2015 when the intermittent mode was used (i.e. not during IOPs). As stated above, the intermittent mode consists of 30 minutes of off-zenith scanning for the profile of horizontal wind followed by a 30 minute period of vertical only measurements.

Figure 3.4 shows the wind profile for the 22 June 2015 at 12 UTC and illustrates how wind profiles form different sources may vary. Especially in layers with strong shear (~ 4600 m) discrepancies become obvious. In this case, the wind velocity between varies up to 50 %. In general the agreement between radiosonde and RWP should be significantly smaller (V. Lehmann, personal communication) All the artificial effects on the radar spectra treated in chapter 2.6 depend on the magnitude of the vertical velocity and are therefore affected by an uncertain estimate of the horizontal wind. For example, overestimating the beam width broadening causes exaggerated broadening of the particle scattering peak and therefore a Bragg peak biased towards positive vertical velocities. Underestimating broadening leads to a particle contaminated Bragg peak and a negative biased velocities.
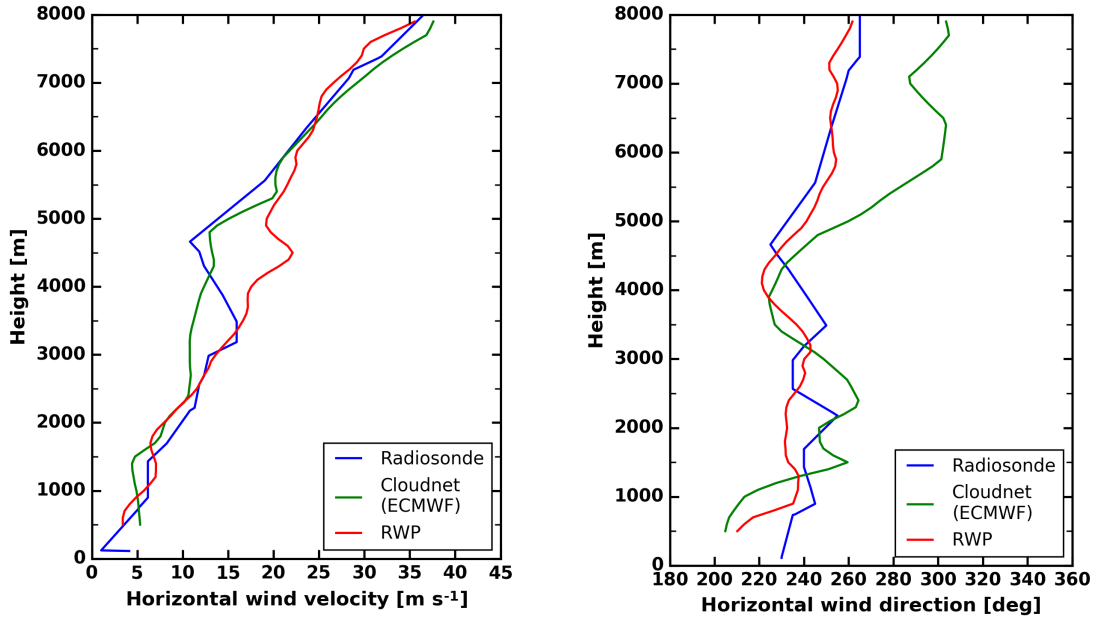
Fig. 3.4: Horizontal wind profiles on the 22 June 2015 at 12 UTC from different sources. Velocity (left) and direction (right).

3.5 Quality control flag

Assessing the quality of the measurement and correction algorithm is a crucial task for automated data processing. A decision logic with threshold was designed in implemented to classify the quality of each spectrum. Potentially unreliable measurements are flagged using a integer-value mask. Figure 3.5 depicts the decision tree.

A spectrum is considered free of particle influence if the reflectivity $Z_{35\,\mathrm{GHz}}$ is smaller than $-25\,\mathrm{dBZ}$ and no atmospheric plankton is present ($LDR_{35\,\mathrm{GHz}} < -13\,\mathrm{dB}$). The reflectivity criterion is based on the theoretical calculations above (see Fig. 2.3). Here a standard peak finding algorithm can be employed. Spectra with low SNR are flagged, but not necessarily masked by an fill value.

When falling particles reach the 0°C isotherm, ice particles start to melt. This melting layer is characterized by high reflectivity $Z_{35\,\mathrm{GHz}} > 0\,\mathrm{dBZ}$ with a $LDR_{35\,\mathrm{GHz}} < -14\,\mathrm{dB}$, an elevated noise level or too many peaks distributed over the frequency range. Within the melting layer the scattering processes are more complicated and a correction with the current algorithm is not possible yet.

All other spectra are corrected for the particle influence by the algorithm described in the former sections. If the estimated vertical velocity is left of the cloud radar peak (i.e. faster downward motion than the falling particles), the spectrum is flagged and, if possible a second peak is used.
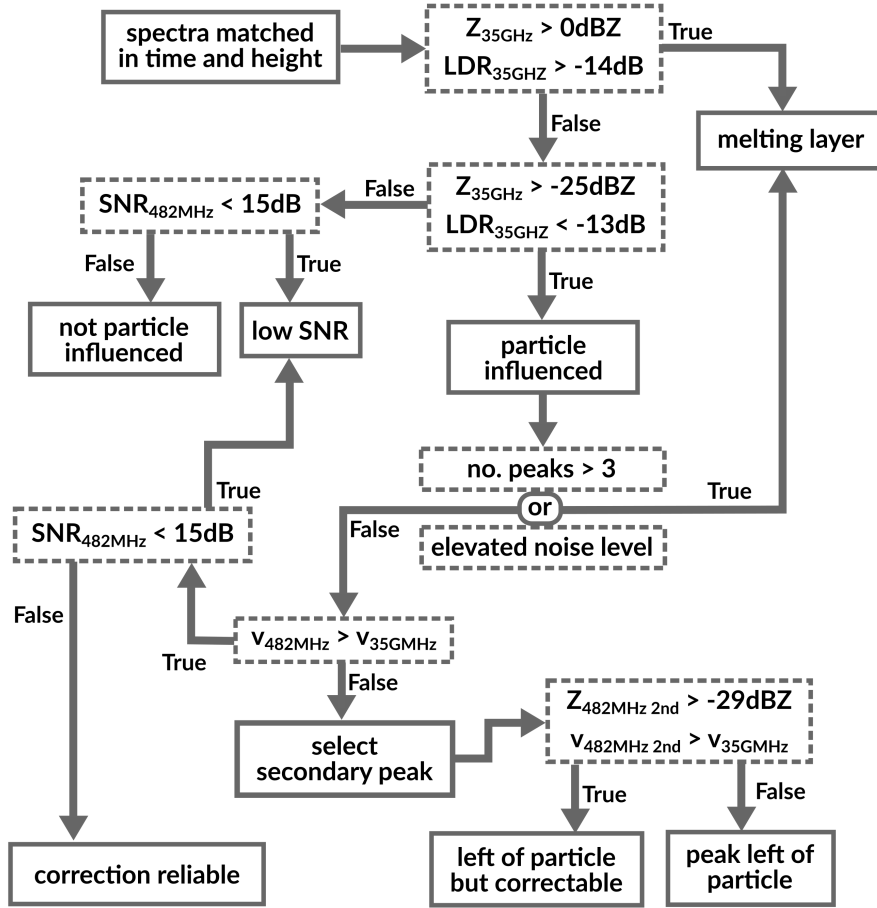
Fig. 3.5: Schematic of the quality flag decision tree. Threshold based decisions are marked by dashed boxes.

3.6 Spectral correction of particle influence on RWP spectra

The correction of the particle influence in the RWP spectra is the core of the proposed combination method and has to be done before vertical air velocity measurements in clouds can be used (see Fig. 2.6). Despite the fact that wind profiler and cloud radar are rather similar, they differ in some technical aspects. This has to be taken into account when the spectral data is combined.

Firstly the range gate length is different (Table 3.1). To obtain a common height resolution, the cloud radar spectra are averaged in height. Different spectral resolutions are matched using linear interpolation. Secondly the beamwidth of the RWP is significantly larger. The larger observation volume is covered by the radar system parameter, but the spectrum is additionally broadened compared to the cloud radar (Section 2.6). The cloud radar spectrum has to be broadened artificially assuming a Gaussian shaped peak with σ_b^2 using equation 2.17.

For the estimation of the RWP Doppler spectrum fewer spectra, than at the cloud radar, are averaged incoherently (Table 3.1). Therefore the estimated spectrum still contains some noise. A running mean with Gaussian shaped window ($\sigma = 1\,\text{pixel}$) is used to smooth the spectrum.

During this work, several methods for the spectral separation were implemented and tested. Three of them are presented in the following section in more detail. Beginning with the straight forward and simple relative spectra. The second approach uses a weighting function and the third one is based on a peak fitting procedure. Afterwards all three methods are evaluated using a Monte Carlo simulation.

3.6.1 Relative spectra

The first approach was to calculate a relative spectrum. Spectral bins influenced by Particle return, the cloud radar and the RWP will observe the same reflectivity. Bins where the RWP signal is stronger, than the cloud radar signal are supposed to be caused by Bragg scattering. Mathematically, this is done by dividing the RWP spectrum through the broadened (see section 2.6 and equation 2.17) cloud radar spectrum. The corrected spectrum is elevated by the wind profiler noise level to preserve the reflectivity. Consecutively, a peak-finding algorithm is employed to the spectrum and the moments (equations 2.14 - 2.16) are calculated.

An example for the correction in precipitation is shown in figure 3.6. The peaks originating from the particle scattering and the Bragg scattering are clearly separated, but the standard RWP peak-finding algorithm is not designed for such multimodal spectra. Therefore, the true shape of the spectrum is not sufficiently represented. Using the corrected spectrum, the vertical velocity is correctly estimated. This rather simple approach works surprisingly well, when Bragg and particle peaks are sufficiently separated (as depicted in figure 3.6). When the Bragg signal is weaker or both peaks are closer together, this corrections method will not perform as desired. So a more sophisticated method are needed.
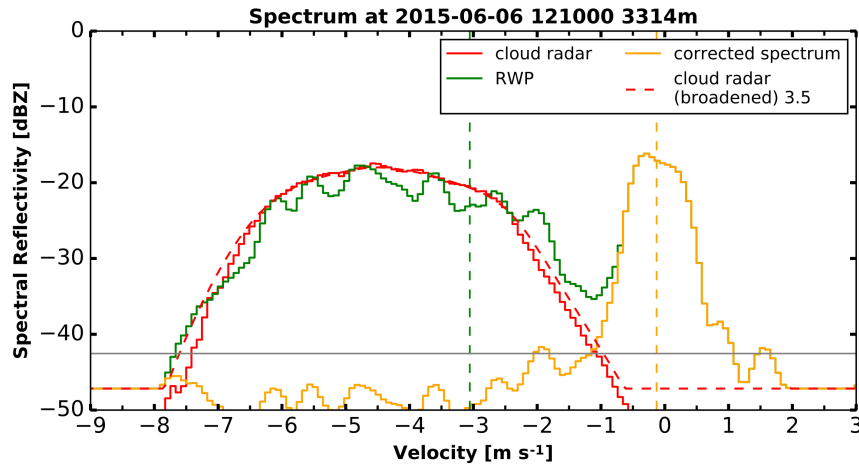

Fig. 3.6: Combined wind profiler and cloud radar spectrum from the 06 June 2015 12:10 UTC at $3314\,\mathrm{m}$. The velocities below $-1\,\mathrm{m\,s^{-1}}$ are caused by precipitation. The peak of Bragg scattering is located at $0\,\mathrm{m\,s^{-1}}$.

3.6.2 Weighting function

The idea for this method is comparable to that proposed by Williams (2012). Here the particle part of the spectrum is suppressed by a weighting function, which is calculated from the cloud radar spectrum. For this study the original approach is refined at several points. The artificial broadening of the spectrum introduced by different beamwidths (Section 2.6) is incorporated. Additionally a more straightforward weighting function is used.

The total reflectivity in each spectral bin is a combination of particle and Bragg signal: $z = z_{\text{Bragg}} + z_{\text{particle}}$. The weighting function is calculated as follows: At fist, the cloud radar spectrum is cut off at the RWP noise level and broadened by σ_b from equation 2.17. The weighting function $\mathcal{P}_{\text{bragg}}$ describes the relative importance of particulate and Bragg scattering:

$$\mathcal{P}_{\text{Bragg}}(v) = 1 - \frac{z_{\text{particle}}(v)}{z_{\text{Bragg}}(v)} \tag{3.1}$$

The weighting function is 1, when the total reflectivity in a bin is dominated by Bragg scattering and 0 when particle scattering dominates. Afterwards this weighting function in filtered with a running mean to suppress noise induced fluctuations. Furthermore $\mathcal{P}_{\text{bragg}} = 1$ is set for all bins where no cloud radar signal is present. After that, the weighting function is scaled by the cloud radar SNR for all weights below a certain threshold.

$$\mathcal{P}_{s\,\text{Bragg}}(v) = [SNR_{35\,\text{GHz}}(v)]^{-1} \text{ for } \mathcal{P}_{\text{Bragg}}(v) < 0.5 \tag{3.2}$$

This reduces the reflectivity in the particle dominated bins down to the noise level. When calculating their weighting function Williams (2012) used a fixed scaling factor of $40\,\text{dB}$. Using the cloud radar SNR provides clearer and more meaningful spectra. The corrected reflectivity spectrum is then calculated by:

$$z_{\text{corr}}(v) = \mathcal{P}_{s\,\text{Bragg}}(v) \cdot z_{482\,\text{MHz}}(v) \tag{3.3}$$

A peak finding algorithm is employed to this spectrum and the moments are calculated (equations 2.14 - 2.16). Figure 3.7 shows an example where the Bragg signal is significantly weaker than the particle return. The weighting functions are also shown.

The accuracy of this method depends strongly on the relative calibration of the RWP and the cloud radar. This issue is addressed with the automated scheme proposed in section 3.3.
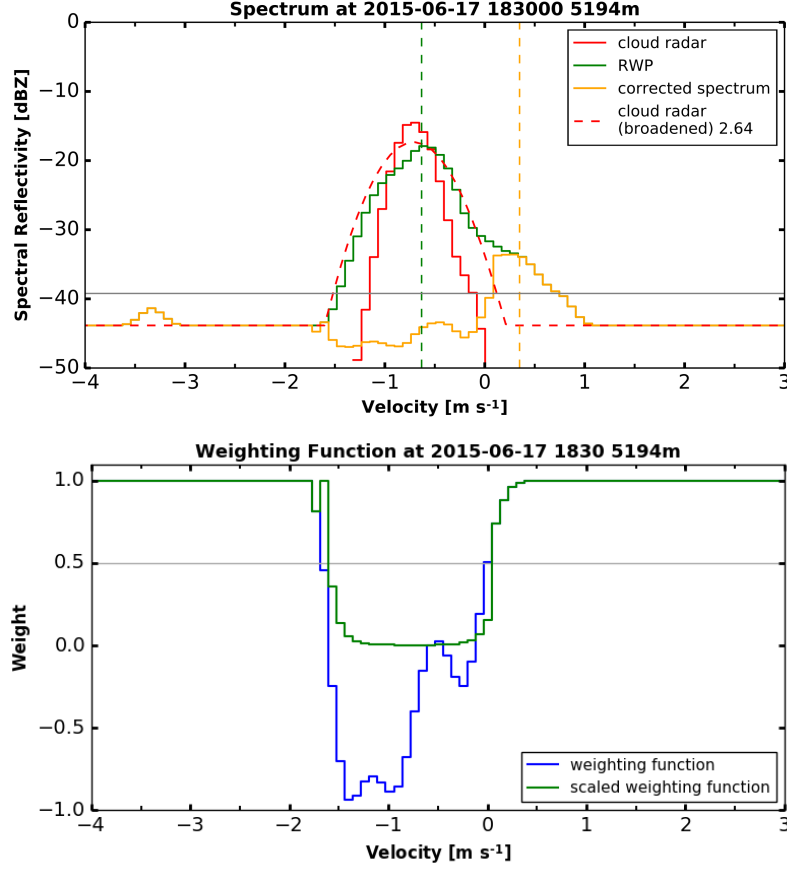
Fig. 3.7: Combined wind profiler and cloud radar spectrum (top) from the 17 June 2015 18:30 UTC at 5194 m. The weighting function for this spectrum is shown in the lower part. The threshold of 0.5 is marked in grey.

3.6.3 Peak fitting

Another method to separate the contributions of Bragg and particle scattering is least squares fitting of two Gaussian peaks. The underlying assumption is, that only the Bragg signal and one particle population contribute to the spectrum. Higher order effects like side lobe return or non-stationarity are not taken into account. Then the signal is modelled as:

$$\hat{s}\left(v_k\right) = \frac{R_{\mathrm{part}}}{\sigma_{\mathrm{part}}\sqrt{2\pi}}\exp\left(-\frac{(v_k - \mu_{\mathrm{part}})^2}{2\,\sigma_{\mathrm{part}}^2}\right) + \frac{R_{\mathrm{B}}}{\sigma_{\mathrm{B}}\sqrt{2\pi}}\exp\left(-\frac{(v_k - \mu_{\mathrm{B}})^2}{2\,\sigma_{\mathrm{B}}^2}\right) \qquad (3.4)$$

The a-priori information for the particle peak is given by the first three moments of the cloud radar spectrum. It is considered to be the leftmost (fastest falling) peak in the spectrum. The second peak is assumed to lie in proximity of $0\,\mathrm{m\,s^{-1}}$. After the fitting procedure, the parameters of the second peak represent the moments of the Bragg peak. Least squares fitting is sensitive to the number and shape of the peaks. If more than two Gaussian shaped peaks are in the spectrum, the fitting may not reproduce the underlying shape.

An example for a successful fit is depicted in Fig. 3.8. Here both peaks have a Gaussian shape, which is nicely covered by the fitted curve. The estimated velocity for the Bragg peak is $0.48\,\mathrm{m\,s^{-1}}$ and for the particle peak $-1.0\,\mathrm{m\,s^{-1}}$.
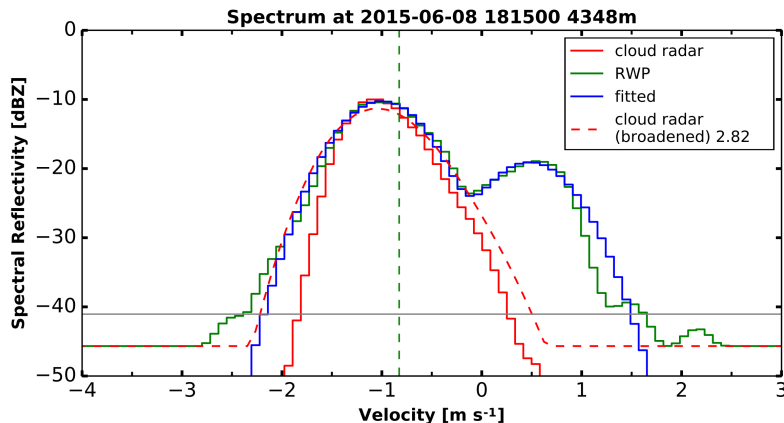

Fig. 3.8: Combined wind profiler and cloud radar spectrum from the 08 June 2015 18:15 UTC at $4348\,\mathrm{m}$.

3.7 Evaluation of the correction methods

Estimating the quality of the correction algorithm is not feasible with an analytical relationship. A Monte Carlo approach is used to assess the accuracy of each proposed method. Cloud radar and RWP spectra are generated synthetically from random input parameters (reflectivity, mean velocity, spectrum width, noise). It is assumed, that both peaks are Gaussian shaped.

A single step in this model consists of the following parts: At first, the input parameters are drawn from a uniform distribution which is restricted by realistic boundaries. Then the synthetic spectrum for the cloud radar (particle peak) and the RWP (particle and Bragg peak) are calculated. Afterwards additive and multiplicative noise is added. A alignment error can also be introduced (Section 2.6). These synthetic spectra are then used as a input for the correction algorithm. The input and output of each Monte Carlo step are saved and is be interpreted statistically afterwards. If the correction algorithm fails to reveal the Bragg peak, this is also saved. So, for each step in the Monte Carlo simulation a new, randomly selected set of input parameters is used to generate the spectra. This validation method is flexible and general. If more methods come up or special configurations should be tested, they can easily be implemented. Additionally, not only the total error can be estimated, but also if it depends on a certain combination of parameters. Two scenarios were set up: one representing precipitation with higher reflectivities and fast downward velocities, the other representing conditions inside a cloud. Here the reflectivities are lower and the downward velocities slower. Details are given in table 3.2.

Parameter	Precipitation	Cloud
$Z_{35\,\text{GHz}}$	$[-18, -5]$	$[-24, -15]$
$v_{35\,\text{GHz}}$	$[-5, -1.5]$	$[-2.5, -0.5]$
$\sigma_{35\,\text{GHz}}$	$[-0.3, -2.0]$	$[-0.2, -1.0]$
$Z_{482\,\text{MHz}}$	$[-20, -10]$	$[-25, -15]$
$v_{482\,\text{MHz}}$	$[-1.0, 1.0]$	$[-1.0, 1.0]$
$\sigma_{482\,\text{GHz}}$	0.5	0.5

Table 3.2: Input settings for the Monte Carlo simulation. The values are artificially chosen, but resemble real atmospheric returns. The units are dBZ and m s^{-1} respectively. Square brackets denote the range from which the random numbers are drawn.

With this model the three different correction methods are evaluated. For each configuration 100000 randomly generated spectra are processed. The error of the corrected velocity estimate is calculated by:

$$v_{\text{err}} = v_{\text{input}} - v_{\text{corr}} \tag{3.5}$$

This error gives an estimate how correct the corrected spectrum represents the artificial Bragg peak and if there is an upward or downward bias. If the estimated vertical velocity is too large, the error becomes negative, indicating a upward bias of the correction. If the error is positive, the estimated velocity is too small. This indicates a downward bias of the correction. As the results of the Monte Carlo simulation show (Table 3.3), the peak fitting method performs best. Both in terms of the velocity error and the proportion of detected peaks. But it has to be considered, that two Gaussian functions are fitted to two Gaussian shaped peaks, which is a strongly simplified assumption. Using real data (which is not necessarily composed of two Gaussian peaks), the portion of cases where the fit fails is higher, than for the other two methods.

Method		Precipitation	Cloud
	not detected	$29.9\,\%$	$26.5\,\%$
relative	mean v_{err}	-0.211	-0.177
	std. dev. v_{err}	0.230	0.440
	not detected	$0.5\,\%$	$1.7\,\%$
fit	mean v_{err}	-0.019	-0.070
	std. dev. v_{err}	0.422	0.458
	not detected	$13.7\,\%$	$15.1\,\%$
weighting function	mean v_{err}	-0.087	-0.059
	std. dev. v_{err}	0.122	0.360

Table 3.3: Results from the Monte Carlo simulation. With v_{err} given in m s^{-1}.

The relative spectra method is the least sensitive to noise and accuracy of the relative calibration, but comes with the largest bias. Furthermore the error depends strongly on the width of the particle peak and the distance of both peaks (Fig. 3.9). The error increases strongly, once a certain width of the particle peak is exceeded. In the cloud scenario, for example this happens at around $0.7\,\mathrm{m\,s^{-1}}$.

Using the weighting function, which is a physically more solid method, the error is smaller. But still it misses the Bragg peak in up to $15\,\%$ of the spectra. Generally the error is smaller for narrow particle peaks and well separated peaks (large distance in the spectrum). It has to be kept in mind that these results rely on idealized spectra with two peaks. Real spectra can be significantly more complex, causing unpredictable errors in the retrieved vertical velocity.
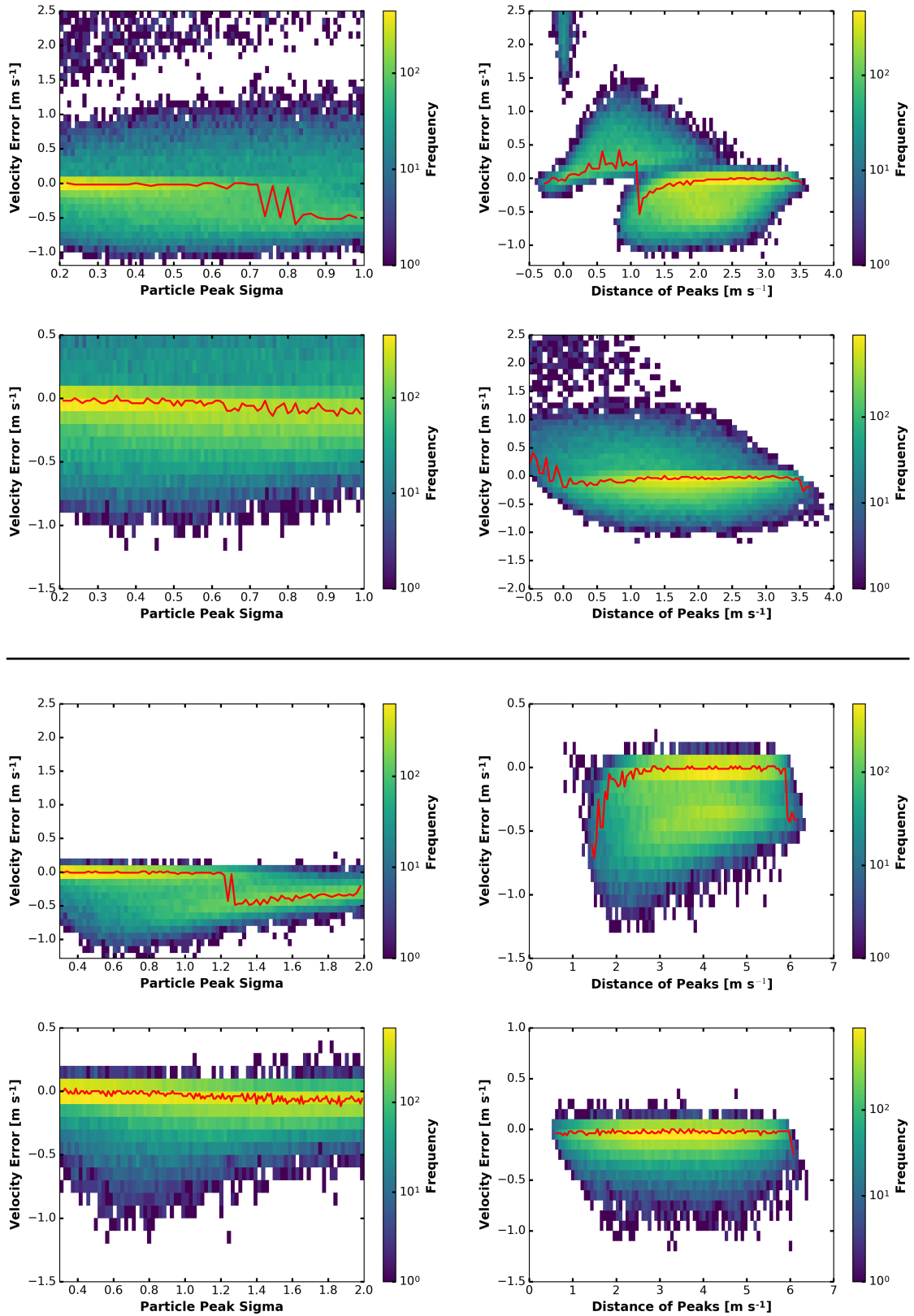
Fig. 3.9: Velocity error for the cloud (upper panel) and precipitation (lower panel) scenario. Depending on the width of the cloud radar peak (left column) and the distance of the peaks (right column) for the relative spectra method (top row in each panel) and the weighting function (bottom row in each panel). The most frequent values highlighted by a red line.

4 Results

In this chapter, the vertical velocity measurements of the COLRAWI campaign are presented. The correction algorithms presented in section 3 is used to gain insight into the vertical air velocity inside clouds. At first, the temporal development of the system parameter is investigated. Afterwards, several cases are discussed in detail, covering the meteorological situation, the measurements and the retrieved vertical air velocities. The cases are selected to show how the collection of measurement instruments performs under various conditions, ranging from cloud free to severe precipitation. ICON simulations of the vertical air motions over the MOL observatory are also presented for one measurement day. After that a comprehensive vertical air velocity statistics, covering the whole campaign, is shown.

4.1 Stability of the relative calibration

As described in Section 3.3 an automated estimation of the system parameter is possible. The daily averages whenever the conditions allowed an estimation are plotted in Fig. 4.1. The overall mean for days with clouds where the intermittent mode was used is 1.42 with a standard deviation of 0.17. This is a variability of less than $1\,\text{dB}$. Relative to each other, both systems are reasonable stable. During the IOPs a different pulse repetition period was used, so these system parameters cannot be directly compared to the intermittent mode. But considering only the IOPs, the relative calibration seems to be quite stable, too.
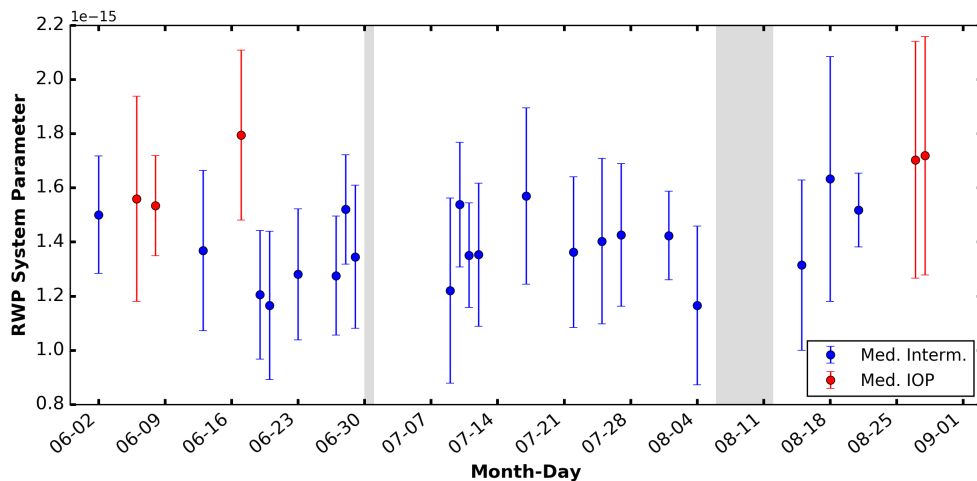

Fig. 4.1: Daily median of the RWP system parameter for the whole campaign whenever appropriate conditions were met. Measurement gaps are marked in grey. The odinate is linearly scaled.

4.2 Case studies

4.2.1 17 June 2015: Warm Front

During the 17 June 2015 an occluding warm front connected to a low pressure system over Iceland crossed northern Germany. This case is shown as first, because here, the particle influence on RWP becomes clearly evident. The first cirrus clouds were present over Lindenberg in the afternoon (Fig. 4.2). During the evening the cloud base height decreased from 10 km to below 3 km at 19 UTC. Due to the relatively dry air below the cloud, the precipitation does not reach the ground until shortly before midnight. The melting layer bright band is located slightly below 3000 m. In areas where no particles are present, the RWP reflectivity reveals layers of strong refractivity gradients. For example the top of the PBL at 2 km and the approaching front (descending from 4 km at 15 UTC to 2 km at 21 UTC) are clearly visible. The vertical velocity (Fig. 4.3) in the free troposphere reveals consecutive up- and downdrafts. In the cloud, the air motion is masked by falling particles. Above the melting layer velocities around $-1\,\mathrm{m\,s^{-1}}$ prevail. Velocities of the liquid particles below range between $-3\,\mathrm{m\,s^{-1}}$ and $-5.5\,\mathrm{m\,s^{-1}}$. Using the correction algorithm vertical velocity information can be obtained even in those areas. The pattern of up- and downdrafts pursues in the rain below the melting layer, whereas in the cloud above, large scale lifting is indicated. The overall pattern is nicely captured by the flag, which allows a quality monitoring of the observed values. Within the melting layer the algorithm works not reliable, so the values are masked with the quality flag "correction unreliable". At some areas within the cloud the refractive index gradients are weak, which results in a low SNR.

Looking at the occurrence of vertical velocities for the whole case (Fig. 4.4), the influence of the particles is clearly visible by the peak at $-1\,\mathrm{m\,s^{-1}}$ in the original data. After using the correction algorithm this peak vanishes. Considering only the particle corrected spectra, a small positive bias remains.

4.2.2 6 June 2015: Deep convection - a weak case

The 6 June 2015 was characterized by a high pressure system over eastern Poland and a low over the Hebrides with a cold front over western Europe. With the Front moving eastward, a convergence zone developed in front of it, triggering some convection. Over Lindenberg the sky was mostly clear with a single shower shortly after 12 UTC. With the RWP information alone it is not possible to identify the areas where particles influence the measurement. The precipitation cloud is wrongly identified as a downdraft, if no additional information is available. Especially if the particles evaporate before reaching the ground, the identification of such events becomes particularly difficult.

In terms of the distribution in this case, the particles only introduce a small skewness, not an extra mode, as in the case presented before (17 June 2015).
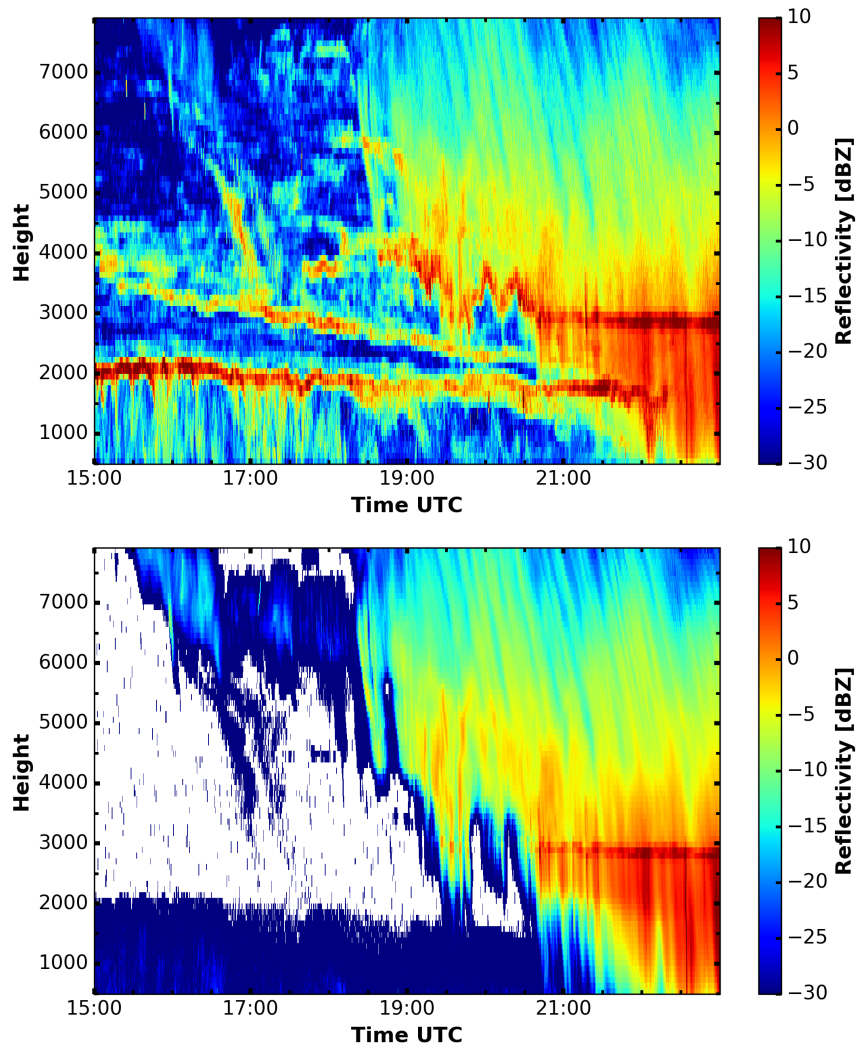
Fig. 4.2: Reflectivity from the RWP (top) and the cloud radar (bottom) during the evening of the 17 June 2015.
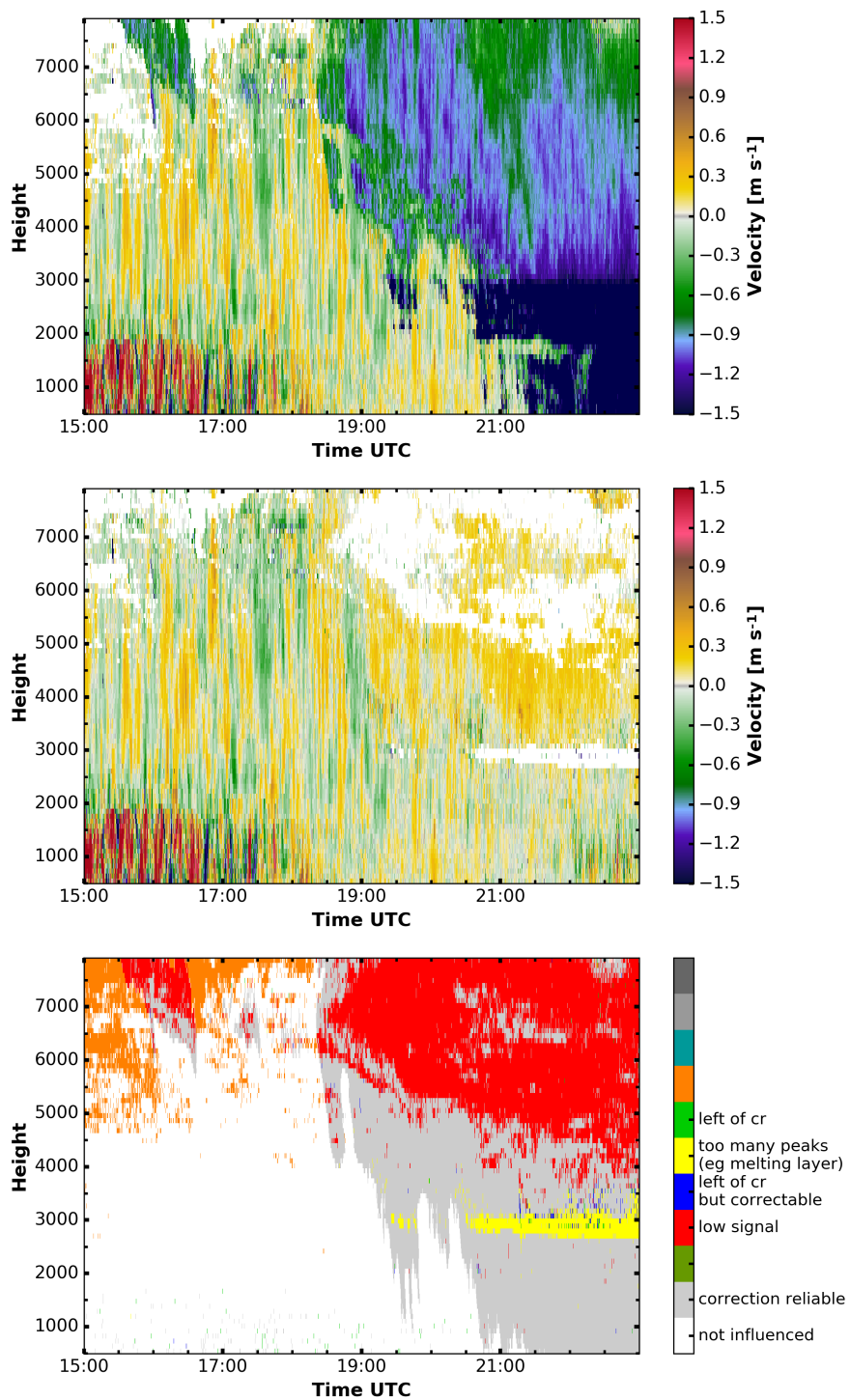
Fig. 4.3: Vertical velocity retrieved with the standard RWP signal processing (top), corrected with the algorithm (middle) and the quality flag (bottom) during the evening of the 17 June 2015. Values exceeding the velocity color scale are shown in dark blue and red, respectively.
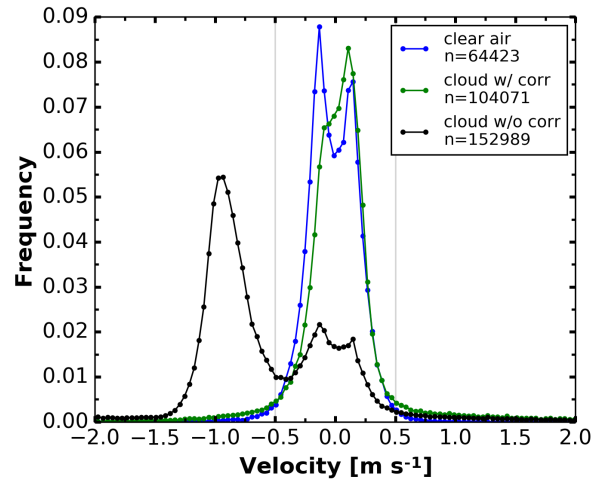
Fig. 4.4: Histogram of the vertical velocities during the evening of the 17 June 2015. The original signal processing/peak finding (black), only the spectra corrected for particle influence (green), only particle free spectra (blue) and all spectra (red).
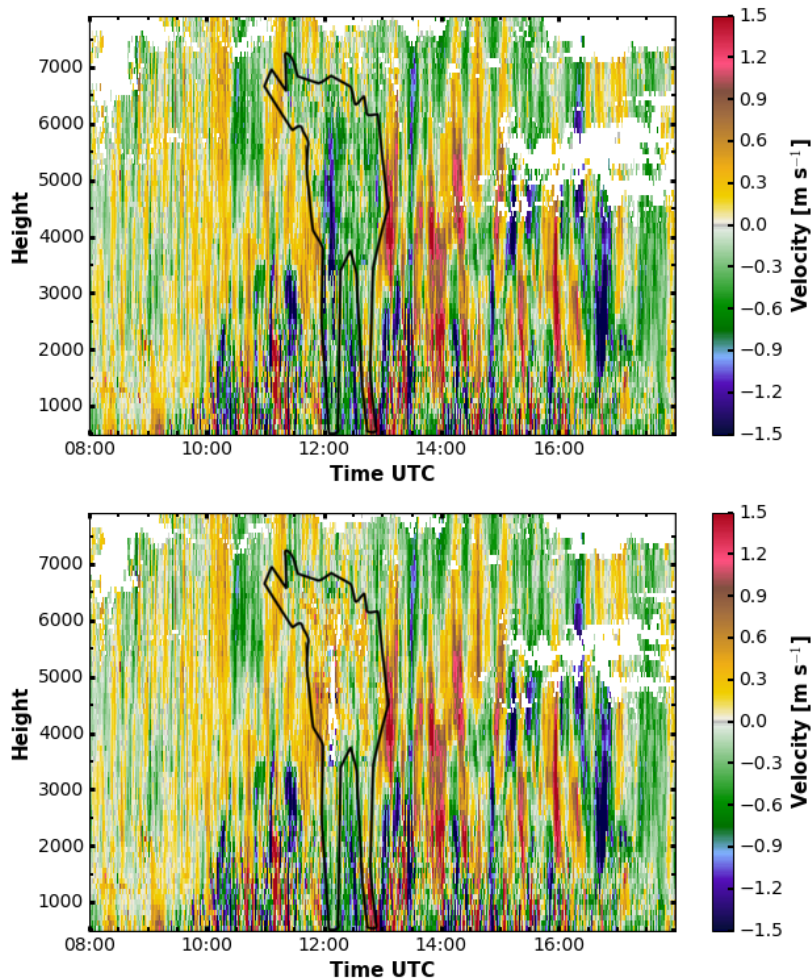

Fig. 4.5: Vertical velocity retrieved with the standard RWP signal processing (top) and corrected with the algorithm (bottom) during the 6 June 2015. The cloud itself is indicated by the black contour line. Values exceeding the velocity color scale are showed in dark blue and red, respectively.

4.2.3 1 August 2015: Mixed phase cloud

On the 1 August 2015 a high pressure system was located over eastern Europe and a low off the coast of Ireland. During the day a small scale low developed over the eastern part of France and moved north-eastward. It advected warmer and moister air massed to eastern Germany. High and mid level clouds were present most of the day. From 15:30 to 17:45 UTC a single layer mixed phase cloud passed over the site (Fig. 4.6). The cloud top height was between 5500 and 6000 m with a temperature around $-16.9°C$. The cloud is split in two parts separated by a short gap at 16:30 UTC. For the first period the liquid water path (LWP) ranged between 70 and $120\,kg\,m^{-2}$, later the LWP peaked at $190\,kg\,m^{-2}$. Within this second part ice production was stronger, forming a clearly visible virga below the liquid layer. As the RWP vertical velocities reveal, the dynamics are a key driver for this cloud. Regrettably are only intermittent mode measurements are available for this case. But is clearly visible that the gap at 16:30 UTC is caused by a downdraft. On the other hand the clouds form or grow, when either the whole cloud or the liquid layer is lifted. It can also be seen, that a short delay exists between the dynamical forcing and the response of the cloud. This example also emphasises the importance of the correction algorithm. In the raw RWP measurement the downward air motion at 16:35 at 3500 m and the virga 20 minutes later at 4500 m could not be distinguished.

4.2.4 13 June 2015: Deep convection - a severe case

On the 13 June 2015 a small low over the North Sea caused strong convective developments over north Germany. During the day labile air masses were advected from south-west and due to dynamical forcing of the low itself strong showers and thunderstorms developed. In the evening two of these convective cells passed over Lindenberg, causing $\sim 20\,mm\,h^{-1}$ precipitation. During this day the RWP was operated in the intermittent mode, so that only 30 min slices of vertical observations are available.

As stated above, cloud radars may suffer from attenuation, especially within convective clouds. Strong attenuation occurred shortly before 18 UTC on this day (Fig. 4.7). Above 2500 m the cloud radar observes no backscattering, as the pulse is attenuated. The RWP is able to observe backscattering within the whole cloud, even well above this height. Maximum reflectivity observed by the cloud radar is 25.2 dBZ, whereas the maximum RWP reflectivity is 50.1 dBZ.

Under these conditions, the vertical air velocity algorithm provides no meaningful results, because the cloud radar signal is no longer available. But the combination of both radars can give valuable information on the cloud itself.
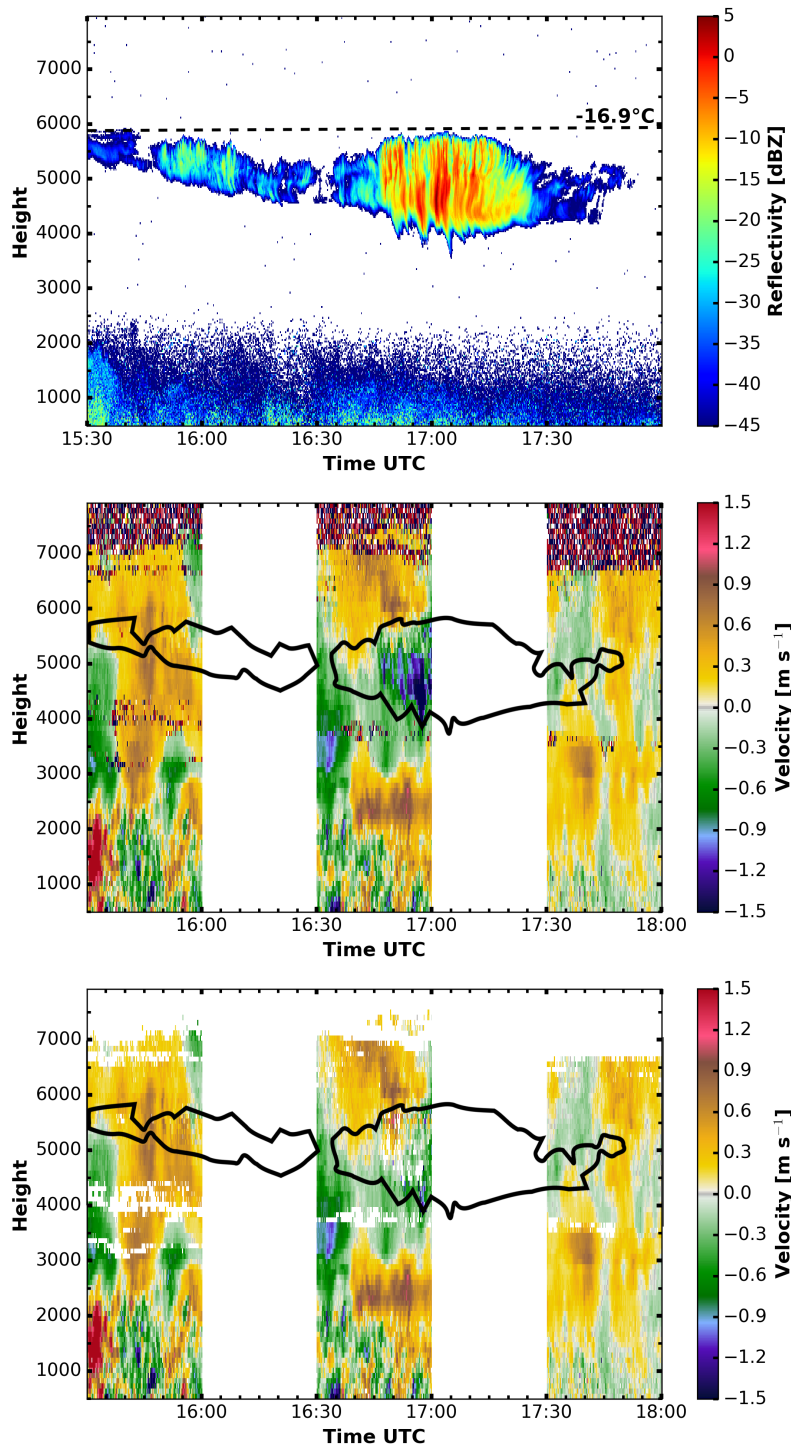
Fig. 4.6: Mixed phase layered cloud on the afternoon to the 1 August 2015. Reflectivity of the cloud radar (top), vertical velocity retrieved with the standard RWP signal processing (middle) and corrected with the algorithm (bottom). Values exceeding the velocity color scale are showed in dark blue and red, respectively.
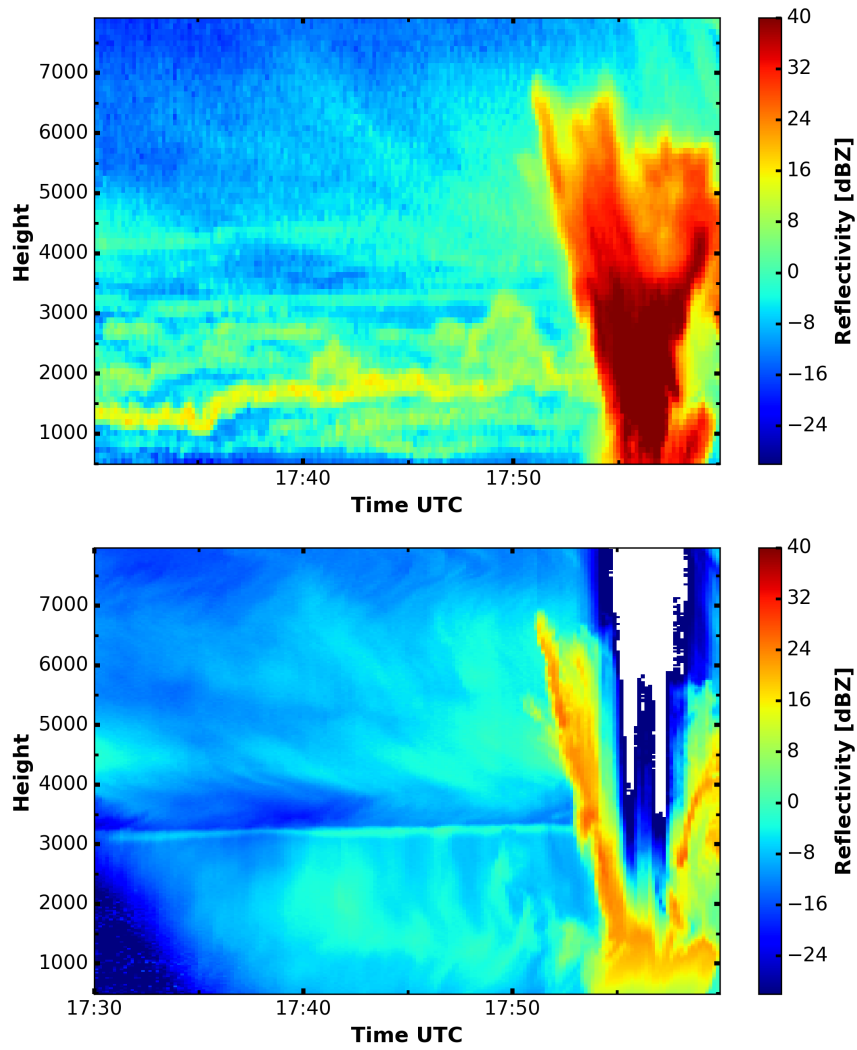
Fig. 4.7: Reflectivity from the RWP (top) and the cloud radar (bottom) during the strong shower at 13 June 2015.

4.3 Comparison with the ICON model

As vertical motions are a key driver of microphysics, the correct representation in NWP and climate models is crucial. It is beyond the scope of this study to evaluate model performance in detail. So, in the following section it is shown exemplarily that velocities obtained from the corrected RWP measurements can be used to asses the representation of vertical motion an turbulence in numerical models. The model used here is the new state-of-the-art model ICON (Zängl et al. 2015) used in the weather forecasting mode by the DWD with a horizontal resolution of 13 km (R03B07 grid). These simulations have been performed by Axel Seifert (DWD).

To match with the model output grid, the measurements have to be averaged to a coarser 10 minutes time grid. As Fig. 4.8 shows, the distribution of vertical velocities differs significantly between model and measurement. The variability is underestimated by the model. The standard deviation in clear air is $0.20\,\mathrm{m\,s^{-1}}$ compared to $0.09\,\mathrm{m\,s^{-1}}$ in the simulation. Within clouds the difference is even larger.
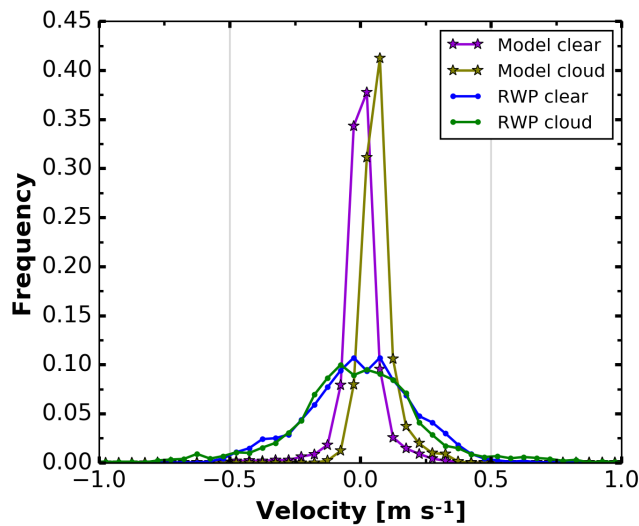

Fig. 4.8: Histogram of the 10 min vertical air velocity at the 27 August 2015 for the ICON model simulation and the averaged RWP measurements.

To determine the turbulent structure, the turbulent energy spectrum is calculated for a measurement period of 30 minutes. An example of such a spectrum is shown in Fig. 4.9. The expected shape is nicely represented. As the Doppler lidar has a higher temporal resolution, its turbulence spectrum extends to higher frequencies. A power law function is fitted to the spectrum for several frequency intervals. Afterwards it is tested, if one of the fits contains a $-5/3$ slope. From its parameters the eddy dissipation rate (EDR) is calculated. The EDR estimation fails when the time interval contains too few valid values or no fit with an appropriate slope exists.
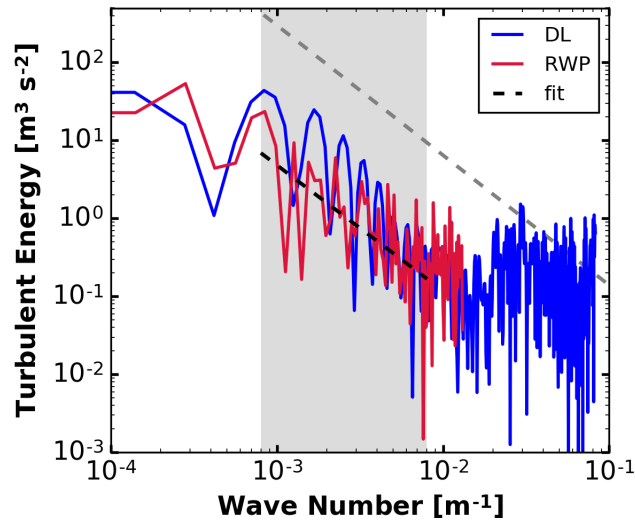
Fig. 4.9: Turbulence spectrum at 4270 m between 15:20 and 15:50 UTC at the 27 August 2015. The theoretical $-5/3$ slope is marked with a dashed gray line. The frequency range where this slope is met by the fit is marked by a gray rectangle and the result of the fit is shown in dashed black.

Figure 4.10 shows the EDR obtained by this method for half a day of measurements. The enhanced turbulence within the PBL is correctly reproduced and also some lifted turbulent layers are visible, especially after 19 UTC. Regrettably, the retrieved EDR could not be compared to the modelled ones, as the turbulent parameter are currently not included in the standard model output.
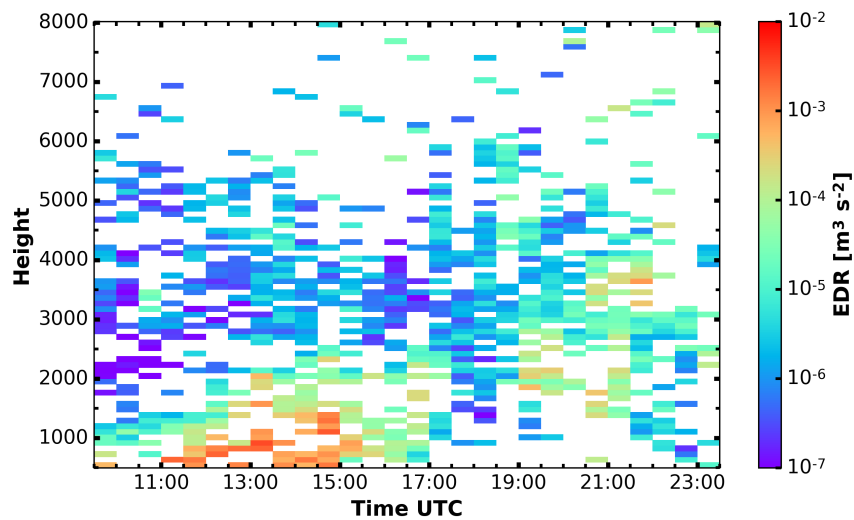

Fig. 4.10: EDR calculated by the described fit algorithm for at the 27 August 2015. White areas indicate regions where either not enough values for the spectrum were present or the slope was not matched.

4.4 Vertical air velocity statistics

The generated vertical air velocity dataset covers several months and allows for a long term statistics of vertical air motion.

Considering the whole campaign, the mean of the vertical velocity without the correction is $-0.296\,\mathrm{m\,s^{-1}}$ (median $-0.102\,\mathrm{m\,s^{-1}}$), whereas the mean with the correction is $-0.017\,\mathrm{m\,s^{-1}}$ (median $-0.005\,\mathrm{m\,s^{-1}}$). Due to mass conservation the long time mean velocity should be $0\,\mathrm{m\,s^{-1}}$. A small downward bias of $-0.05\,\mathrm{m\,s^{-1}}$ caused by vertical propagating gravity waves is possible, as suggested by Nastrom and VanZandt (1994) Hence, even in the long term statistics, the particle influence becomes visible. A clear secondary peak caused by particles is also present in the histogram (Fig. 4.11) centered at $-1\,\mathrm{m\,s^{-1}}$. Within clouds the mean vertical motion without correction is $-0.662\,\mathrm{m\,s^{-1}}$ (median $-0.309\,\mathrm{m\,s^{-1}}$) and with correction $-0.035\,\mathrm{m\,s^{-1}}$ (median $-0.013\,\mathrm{m\,s^{-1}}$).

Not only the magnitude of the vertical velocity is relevant for cloud microphysics, but also the variability. The standard derivation of the vertical air velocity (clear air and cloud) is $-0.411\,\mathrm{m\,s^{-1}}$, compared to $-0.926\,\mathrm{m\,s^{-1}}$ for the uncorrected velocities. This means, that the particle influence artificially broadens the distribution.
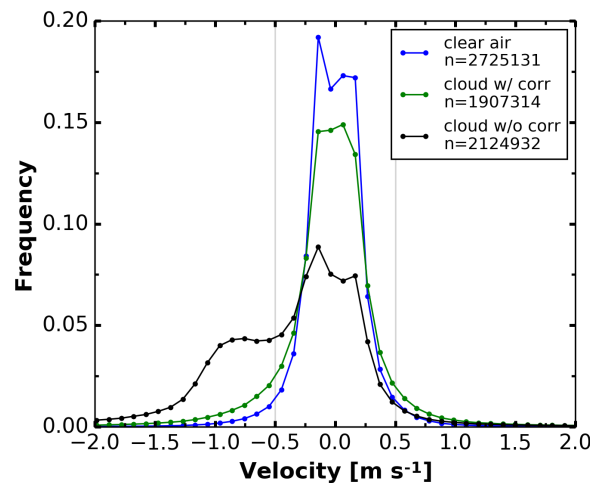

Fig. 4.11: Histogram of the vertical velocities for the whole campaign. The RWP-only signal processing/peak finding (black), the spectra corrected for particle influence (green), only particle free spectra (blue). n denotes the number of measurements, that contributed to the histogram.

Looking at the height resolved statistics (Table 4.1) it becomes obvious, that for the clear air cases the vertical air velocity is close to $0\,\mathrm{m\,s^{-1}}$ at all height bins with deviations of less than $0.025\,\mathrm{m\,s^{-1}}$. The standard deviation generally decreases with height. Within clouds, the mean air velocity is also close to zero with deviations of less than $0.066\,\mathrm{m\,s^{-1}}$. But variability is higher. This becomes also obvious, when considering the height-resolved histogram (Fig. 4.12). For the uncorrected signal, ice particles strongly influence the velocity towards negative values above $3500\,\mathrm{m}$ and liquid precipitation below that. After correction, the median is close to that of clear air at all heights.

Category	0 - 2.5 km		2.5 - 5 km		>5 km	
	v	σ	v	σ	v	σ
clear air	-0.025	0.318	-0.002	0.268	$+0.002$	0.264
cloud w/ correction	-0.030	0.570	-0.066	0.553	-0.002	0.368
cloud w/o correction	-0.765	1.615	-0.702	1.096	-0.471	0.506
clear air + cloud w/ correction	-0.027	0.486	-0.020	0.390	$+0.001$	0.328
clear air + cloud w/o correction	-0.467	1.316	-0.222	0.735	-0.195	0.467

Table 4.1: Height resolved statistics for the vertical air velocity in $\mathrm{m\,s^{-1}}$. Shown is the mean (v) and standard deviation (σ) of the vertical velocity.

The spectral width (second moment of the Doppler spectrum) is a proxy for small scale variability of the vertical velocity. In the case of clear air, the mean spectral width is $0.267\,\mathrm{m\,s^{-1}}$ and within clouds $0.288\,\mathrm{m\,s^{-1}}$. But the 90th percentile inside clouds is $0.423\,\mathrm{m\,s^{-1}}$ compared to $0.372\,\mathrm{m\,s^{-1}}$. Hence, larger spectral widths are more common within clouds.
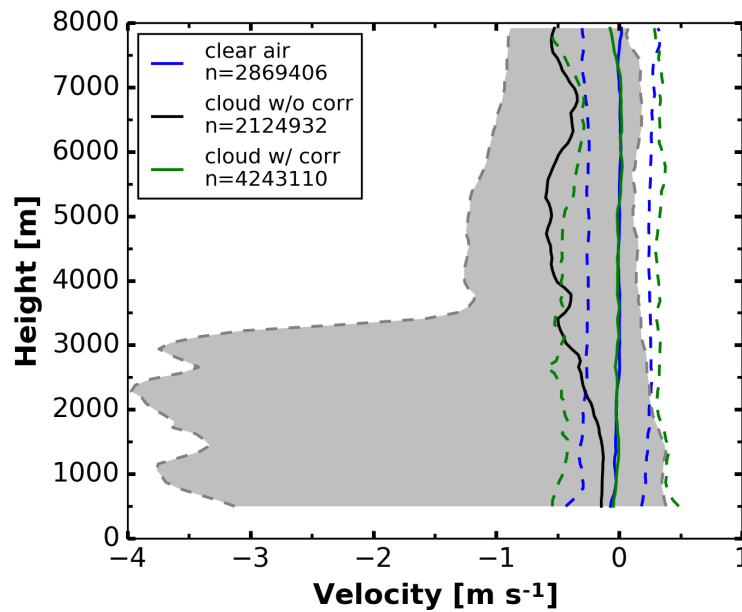

Fig. 4.12: Profile of the vertical air velocity histogram with the 10th (dashed), 50th (solid) and 90th (dashed) percentile. The 10th to 90th percentile of the in-cloud air velocity without correction is shaded in grey.

5 Summary and Discussion

In this work, it has been shown that a 482 MHz RWP can provide observations of vertical air motion even within clouds. To overcome the windprofiler ambiguity, which may mask the vertical air motion when particles are present, the Doppler spectra of the RWP and a a 35 GHz cloud radar were combined. An algorithm for the combination of both instruments and the correction of the ambiguity was designed, implemented and tested. Furthermore data quality control scheme and a relative calibration procedure was developed to make an automated setup within the Cloudnet framework possible. This makes vertical air motion observations in the free troposphere available within this framework.

The algorithm with three correction methods (Section 3.6) was evaluated, using a Monte Carlo approach (Section 3.7). A Monte Carlo approach has been found necessary, because in such a complex algorithm, errors do not propagate linearly. It was found, that the weighting function approach gives the best results with an error in the velocity estimate of less than $-0.09\,\mathrm{m\,s^{-1}}$. For spectra, where fitting is successful, the error is much smaller ($-0.02\,\mathrm{m\,s^{-1}}$). For spectra with more than two peak or non Gaussian shape, this error will be larger, but cannot be covered by the current simulation.

The horizontal wind may distort the spectra, as it was shown in section 2.6. To take this effects into account, profiles of the horizontal wind with a vertical resolution in the order of hundred meters are required. The temporal spacing need be sufficient to cover changes of the meteorological conditions. Taking into account radiosondes, model data and the RWP horizontal wind measurement mode, no source without disadvantages could be found (Section 3.4). The best compromise to get a highly resolved profile of horizontal wind and vertical measurements seems to be the intermittent mode of the RWP. But it comes at the cost of gaps in vertical observations.

The developed algorithm was applied to the data from the COLRAWI campaign at MOL (Section 4). It was shown that the relative calibration is stable within a standard deviation of less than 1 dB for the three month period in 2015. Hence, either the power of both instruments fluctuates in phase or they are quite stable. This allows no estimation of the absolute accuracy of the calibration, but shows that the relative calibration method is applicable when combining measurements of both instruments.

Using single cases, the performance of the combination and correction algorithm was illustrated for conditions ranging from clear air to severe convection. At each case, the RWP provides valuable additional information on clouds and dynamics. Using the combination of both instruments, areas where Bragg and particle scattering interfere can be detected and the particle influence can be corrected (Sections 4.2.1 and 4.2.2). The vertical air velocity dataset can be used to investigate cloud-dynamics interactions (Section 4.2.3). Relative calibration of the RWP using the cloud radar allows quantitative measurements of radar reflectivity in severe precipitation, where the cloud radar is al-

ready attenuated (Section 4.2.4). Hence, a gap of measurements that so far existed in the cloud radar observations can be filled, meaning that cloud radar and RWP together can deliver useful data about clouds under nearly all conceivable weather situations.

This continuous observations of vertical air velocities also offer new opportunities regarding NWP model evaluation (Section 4.3). The representation of vertical air motion in the model depends strongly on the resolution and the set of parametrisations used. Hence, a direct comparison is not particularly useful. But a long-term dataset of vertical air motion within the framework of Cloudnet offers various opportunities for model evaluation.

Considering the whole dataset (Section 4.4), the mean vertical air velocity was found to be $-0.017\,\mathrm{m\,s^{-1}}$. The expected long-term averaged vertical air velocity is close $0\,\mathrm{m\,s^{-1}}$, due to the conservation of mass. Within the retrieval uncertainty and a possible bias due to propagating gravity waves, the expected value is matched. So the particle influence is not only relevant when looking at single clouds, but also on a larger temporal scale. This becomes evident when comparing the mean vertical air motion inside clouds with correction $(-0.031\,\mathrm{m\,s^{-1}})$ and without $(-0.662\,\mathrm{m\,s^{-1}})$. For the first time a long-term evaluation of vertical air velocities, even on the scale of NWP models is possible.

The standard deviation of the vertical air velocity was found to be $0.411\,\mathrm{m\,s^{-1}}$ when all conditions are considered. Within clouds the standard deviation is $0.528\,\mathrm{m\,s^{-1}}$ and therefore slightly higher, than in clear air $(0.280\,\mathrm{m\,s^{-1}})$.

6 Outlook

It was shown, that removing the influence of particles on RWP measurements is possible and that in many cases the Bragg signal is unambiguously revealed. This opens the opportunity for further studies, especially investigations of aerosol-cloud-dynamics interaction. For example the approach used by Bühl et al. (2016) could be used to investigate vertical motion connected to shallow mixed phase clouds. Long term observations can also be used to evaluate the accuracy of vertical dynamics in NWP models.

But the algorithm itself can be further improved. At first it became evident that an averaging time of 10 s is too coarse for the observation of small scale fluctuations with two radars. In the worst case two spectra are recorded 5 s apart, which is too much for short scale dynamics. Secondly the Doppler spectrum itself is computed using assumptions, like signal stationarity, that are not fulfilled at any time. For those situations it is misleading to look only at the Doppler spectrum. Both limitations could be addressed using employing a custom *I-Q* processor, meaning that both radars are combined in an earlier step of the signal processing (Section 2.5). For this, the the recording of the periodograms or even *I-Q* data at both instruments is necessary. The amount of data that has to be stored would increase by a factor of 10 to 100 compared to the Doppler spectra or up to 1000 compared to the moments. A compromise could be a dynamic decision in the real time data processing, whether to save these data. The decision could be based for example on signal stationarity or returned power.

Appreciating that Cloudnet is a valuable tool for long term observations, model evaluation and retrieval of cloud microphysics, some improvements are possible. At least on campaign basis coordinated time slots for scanning are necessary to obtain information on particle shape (Myagkov et al. 2016) or horizontal wind profiles (RWP and scanning Doppler lidar). Considering the combination of RWP and cloud radar the intermittent mode seems to be a reasonable compromise, but longer periods for vertical measurements would be desirable.

Bibliography

Argyrouli, A., N. Budko, H. Russchenberg, and C. Unal. 2012. "The effect of droplet clustering on the statistics of radar backscatter from water clouds." In *Proc. Ninth Int. Symp. on Tropospheric Profiling.* L'Aquila, Italy.

Balsley, B. B., and K. S. Gage. 1982. "On the use of radars for operational wind profiling." *Bulletin of the American Meteorological Society* 63, no. 9 (September): 1009–1018. doi:10.1175/1520-0477(1982)063<1009:OTUORF>2.0.CO;2.

Bauer-Pfundstein, M. R., and U. Görsdorf. 2007. "Target separation and classification using cloud radar Doppler-spectra." In *Proceedings of the 33rd Conference on Radar Meteorology,* vol. 880.

Böhme, T., T. Hauf, and V. Lehmann. 2004. "Investigation of short-period gravity waves with the Lindenberg 482 MHz tropospheric wind profiler." *Quarterly Journal of the Royal Meteorological Society* 130, no. 603 (October 1): 2933–2952.

Bohren, C. F., and D. R. Huffman. 2008. *Absorption and scattering of light by small particles.* John Wiley & Sons.

Bony, S., B. Stevens, D. M. Frierson, C. Jakob, M. Kageyama, R. Pincus, T. G. Shepherd, S. C. Sherwood, A. P. Siebesma, A. H. Sobel, et al. 2015. "Clouds, circulation and climate sensitivity." *Nature Geoscience* 8 (4): 261–268.

Bühl, J. 2015. "Combined lidar and radar observations of vertical motions and heterogeneous ice formation in mixed-phase layered clouds." PhD diss., University Leipzig.

Bühl, J., R. Leinweber, U. Görsdorf, M. Radenz, A. Ansmann, and V. Lehmann. 2015. "Combined vertical-velocity observations with Doppler lidar, cloud radar and wind profiler." *Atmospheric Measurement Techniques* 8 (8): 3527–3536.

Bühl, J., R. Engelmann, and A. Ansmann. 2012. "Removing the laser-chirp influence from coherent doppler lidar datasets by two-dimensional deconvolution." *Journal of Atmospheric and Oceanic Technology* 29, no. 8 (August): 1042–1051. doi:10.1175/JTECH-D-11-00144.1.

Bühl, J., P. Seifert, A. Myagkov, and A. Ansmann. 2016. "Measuring ice- and liquid-water properties in mixed-phase cloud layers at the Leipzig Cloudnet station." *Atmospheric Chemistry and Physics* 16, no. 16 (August 26): 10609–10620. doi:10.5194/acp-16-10609-2016.

Donner, L. J., T. A. O'Brien, D. Rieger, B. Vogel, and W. F. Cooke. 2016. "Are atmospheric updrafts a key to unlocking climate forcing and sensitivity?" *Atmospheric Chemistry and Physics* 16, no. 20 (October 20): 12983–12992. doi:`10.5194/acp-16-12983-2016`.

Doviak, R. J., and D. S. Zrnic. 1993. *Doppler radar & weather observations.* Academic Press.

Gage, K. S., C. R. Williams, and W. L. Ecklund. 1994. "UHF wind profilers: A new tool for diagnosing tropical convective cloud systems." *Bulletin of the American Meteorological Society* 75, no. 12 (December): 2289–2294.

Gage, K. S., C. R. Williams, W. L. Ecklund, and P. E. Johnston. 1999. "Use of two profilers during MCTEX for unambiguous identification of Bragg scattering and Rayleigh scattering." *Journal of the Atmospheric Sciences* 56, no. 21 (November): 3679–3691.

Giangrande, S. E., D. M. Babb, and J. Verlinde. 2001. "Processing millimeter wave profiler radar spectra." *Journal of Atmospheric and Oceanic Technology* 18, no. 9 (September): 1577–1583. doi:`10.1175/1520-0426(2001)018<1577:PMWPRS>2.0.CO;2`.

Görsdorf, U., V. Lehmann, M. Bauer-Pfundstein, G. Peters, D. Vavriv, V. Vinogradov, and V. Volkov. 2015. "A 35-GHz Polarimetric Doppler radar for long-term observations of cloud parameters — description of system and data processing." *Journal of Atmospheric and Oceanic Technology* 32, no. 4 (April): 675–690.

Hardy, K. R., D. Atlas, and K. M. Glover. 1966. "Multiwavelength backscatter from the clear atmosphere." *Journal of Geophysical Research* 71 (6): 1537–1552.

Heymsfield, A., and C. Westbrook. 2010. "Advances in the estimation of ice particle fall speeds using laboratory and field measurements." *Journal of the Atmospheric Sciences* 67 (8): 2469–2482.

Hildebrand, P. H., and R. Sekhon. 1974. "Objective determination of the noise level in Doppler spectra." *Journal of Applied Meteorology* 13 (7): 808–811.

Illingworth, A., R. Hogan, E. O'connor, D. Bouniol, et al. 2007. "Cloudnet." *Bulletin of the American Meteorological Society* 88 (6): 883.

Knight, C. A., and L. J. Miller. 1998. "Early radar echoes from small, warm cumulus: Bragg and hydrometeor scattering." *Journal of the atmospheric sciences* 55 (18): 2974–2992.

Kolmogorov, A. N. 1941. "The local structure of turbulence in incompressible viscous fluid for very large Reynolds numbers." In *Dokl. Akad. Nauk SSSR,* 30:301–305. 4. JSTOR.

Korolev, A. 2007. "Limitations of the Wegener-Bergeron-Findeisen mechanism in the evolution of mixed-phase clouds." *Journal of the Atmospheric Sciences* 64 (9): 3372–3375.

Korolev, A., and P. R. Field. 2008. "The effect of dynamics on mixed-phase clouds: Theoretical considerations." *Journal of the Atmospheric Sciences* 65 (1): 66–86.

Korolev, A., and G. Isaac. 2003. "Phase transformation of mixed-phase clouds." *Quarterly Journal of the Royal Meteorological Society* 129, no. 587 (January 1): 19–38. doi:`10.1256/qj.01.203`.

Lehmann, V. 2010. "Wind profilers radars (COST Wind Initiative for a Network Demonstration in Europe: CWINDE network)." In *TECO-2010 - WMO Technical Conference on Meteorological and Environmental Instruments and Methods of Observation.* World Meteorological Organization. `http://www.wmo.int/pages/prog/www/IMOP/publications/IOM-104_TECO-2010/2_Keynote_2_Lehmann.pdf`.

Matsuda, K., R. Onishi, M. Hirahara, R. Kurose, K. Takahashi, and S. Komori. 2014. "Influence of microscale turbulent droplet clustering on radar cloud observations." *Journal of the Atmospheric Sciences* 71, no. 10 (October): 3569–3582. doi:`10.1175/JAS-D-13-0368.1`.

Mitchell, D. L. 1996. "Use of mass-and area-dimensional power laws for determining precipitation particle terminal velocities." *Journal of the atmospheric sciences* 53 (12): 1710–1723.

Muschinski, A., V. Lehmann, L. Justen, and G. Teschke. 2005. "Advanced radar wind profiling." *Meteorologische Zeitschrift* 14, no. 5 (October 1): 609–625. doi:`10.1127/0941-2948/2005/0067`.

Muschinski, A., and P. P. Sullivan. 2013. "Using large-eddy simulation to investigate intermittency fluxes of clear-air radar reflectivity in the atmospheric boundary layer," 2321–2322. IEEE, July. Accessed February 16, 2017. doi:`10.1109/APS.2013.6711819`. `http://ieeexplore.ieee.org/document/6711819/`.

Myagkov, A., P. Seifert, M. Bauer-Pfundstein, and U. Wandinger. 2016. "Cloud radar with hybrid mode towards estimation of shape and orientation of ice crystals." *Atmospheric Measurement Techniques* 9 (2): 469–489.

Nastrom, G. D. 1997. "Doppler radar spectral width broadening due to beamwidth and wind shear." *Annales Geophysicae* 15 (6): 786–796.

Nastrom, G. D., and T. E. VanZandt. 1994. "Mean vertical motions seen by radar wind profilers." *Journal of Applied Meteorology* 33, no. 8 (August): 984–995. doi:`10.1175/1520-0450(1994)033<0984:MVMSBR>2.0.CO;2`.

Orr, B. W., and B. E. Martner. 1996. "Detection of weakly precipitating winter clouds by a NOAA 404-MHz wind profiler." *Journal of Atmospheric and Oceanic Technology* 13, no. 3 (June): 570–580.

Ottersten, H. 1969. "Atmospheric structure and radar backscattering in clear air." *Radio Science* 4 (12): 1179–1193.

Pearson, G., F. Davies, and C. Collier. 2009. "An analysis of the performance of the UFAM pulsed Doppler lidar for observing the boundary layer." *Journal of Atmospheric and Oceanic Technology* 26, no. 2 (February): 240–250. doi:10.1175/2008JTECHA1128.1.

Ramanathan, V., R. D. Cess, E. F. Harrison, P. Minnis, B. R. Barkstrom, E. Ahmad, and D. Hartmann. 1989. "Cloud-radiative forcing and climate: Results from the Earth Radiation Budget Experiment." *Science* 243, no. 4887 (January 6): 57–63. doi:10.1126/science.243.4887.57.

Ramanathan, V., P. Crutzen, J. Kiehl, and D. Rosenfeld. 2001. "Aerosols, climate, and the hydrological cycle." *Science* 294 (5549): 2119–2124.

Ray, P. S. 1972. "Broadband complex refractive indices of ice and water." *Applied Optics* 11 (8): 1836–1844.

Reichardt, J., U. Wandinger, V. Klein, I. Mattis, B. Hilber, and R. Begbie. 2012. "RAMSES: German Meteorological Service autonomous Raman lidar for water vapor, temperature, aerosol, and cloud measurements." *Applied Optics* 51, no. 34 (December 1): 8111. doi:10.1364/AO.51.008111.

Reinking, R. F., S. Y. Matrosov, R. T. Bruintjes, and B. E. Martner. 1997. "Identification of hydrometeors with elliptical and linear polarization K_a-Band radar." *Journal of Applied Meteorology* 36, no. 4 (April): 322–339. doi:10.1175/1520-0450(1997)036<0322:IOHWEA>2.0.CO;2.

Reutter, P., H. Su, J. Trentmann, M. Simmel, D. Rose, S. Gunthe, H. Wernli, M. Andreae, and U. Pöschl. 2009. "Aerosol-and updraft-limited regimes of cloud droplet formation: influence of particle number, size and hygroscopicity on the activation of cloud condensation nuclei (CCN)." *Atmospheric Chemistry and Physics* 9 (18): 7067–7080.

Rinehart, R. E. 1991. "Radar for Meteoroiogists I."

Shupe, M. D., P. Kollias, M. Poellot, and E. Eloranta. 2008. "On deriving vertical air motions from cloud radar Doppler spectra." *Journal of Atmospheric and Oceanic Technology* 25 (4): 547–557.

Van Zandt, T. E. 2000. "A brief history of the development of wind-profiling or MST radars." *Annales Geophysicae* 18 (7): 740–749.

Werner, C. 2005. "Doppler wind lidar." In *Lidar Range-Resolved Optical Remote Sensing of the Atmosphere.* Springer Series in Optical Sciences 102. New York: Springer-Verlag.

Williams, C. R. 2012. "Vertical air motion retrieved from dual-frequency profiler observations." *Journal of Atmospheric and Oceanic Technology* 29, no. 10 (October): 1471–1480. doi:10.1175/JTECH-D-11-00176.1.

Williams, C. R., W. L. Ecklund, P. E. Johnston, and K. S. Gage. 2000. "Cluster analysis techniques to separate air motion and hydrometeors in vertical incident profiler observations." *Journal of Atmospheric and Oceanic Technology* 17, no. 7 (July): 949–962.

Williams, K., and G. Tselioudis. 2007. "GCM intercomparison of global cloud regimes: present-day evaluation and climate change response." *Climate Dynamics* 29, no. 2 (June 6): 231–250. doi:10.1007/s00382-007-0232-2.

Woodman, R. F., and A. Guillen. 1974. "Radar observations of winds and turbulence in the Stratosphere and Mesosphere." *Journal of the Atmospheric Sciences* 31, no. 2 (March): 493–505. doi:10.1175/1520-0469(1974)031<0493:ROOWAT>2.0.CO;2.

Zängl, G., D. Reinert, P. Rípodas, and M. Baldauf. 2015. "The ICON (ICOsahedral Non-hydrostatic) modelling framework of DWD and MPI-M: Description of the non-hydrostatic dynamical core." *Quarterly Journal of the Royal Meteorological Society* 141, no. 687 (January): 563–579. doi:10.1002/qj.2378.

List of acronyms

RWP   radar wind profiler

SNR   signal to noise ratio

CCN   cloud condensation nuclei

IN   ice nuclei

LWP   liquid water path

PBL   planetary boundary layer

IF   intermedient frequency

EDR   eddy dissipation rate

NWP   numerical weather prediction

ACTRIS   Aerosol, Clouds and Trace gases Research Infrastructure

MOL   Meteorological Observatory Lindenberg

UTC   Universal Time Coordinated

LT   Local Time

IOP   intensive observation period

DWD   Deutscher Wetterdienst (German Meteorological Service)

Selbstständigkeitserklärung

Hiermit erkläre ich, dass ich die vorliegende Arbeit selbständig verfasst habe und keinerlei außer den angegebenen Hilfsmitteln oder Quellen verwendet habe. Jegliche verwendete Literatur oder anderweitige Quelle wurde als solche gekennzeichnet und zitiert. Alle abgebildeten Grafiken, sofern sie nicht mit einem Quellenvermerk versehen sind, wurden von mir selbst erstellt. Des Weiteren wurde diese Arbeit noch nie in gleicher oder ähnlicher Form bei einer anderen Prüfungsbehörde eingereicht. Ich erkläre mich damit einverstanden, eine positive Bewertung der Arbeit vorausgesetzt, dass Kopien dieser Arbeit in der Bücherei der Fakultät für Physik und Geowissenschaften der Universität Leipzig sowie am Leibniz Institut für Troposphärenforschung in Leipzig zur Verfügung gestellt werden.

Leipzig, 26.2.2017 _____

Martin Radenz